Alteration trends and geochemical source region characteristics preserved in the fluviolacustrine sedimentary record of Gale crater, Mars

Available online at www.sciencedirect.com

ScienceDirect

Geochimica et Cosmochimica Acta 246 (2019) 234–266

Geochimica et Cosmochimica Acta

www.elsevier.com/locate/gca

Alteration trends and geochemical source region characteristics preserved in the fluviolacustrine sedimentary record of Gale crater, Mars

C.C. Bedford [a,*], J.C. Bridges [b], S.P. Schwenzer [c], R.C. Wiens [d], E.B. Rampe [e], J. Frydenvang [f], P.J. Gasda [d]

[a] School of Physical Sciences, The Open University, Walton Hall, Milton Keynes MK7 6AA, UK
[b] Space Research Centre, Dept. of Physics and Astronomy, University of Leicester, Leicester LE1 7RH, UK
[c] School of Environment, Earth and Ecosystem Sciences, The Open University, Walton Hall, Milton Keynes MK7 6AA, UK
[d] Los Alamos National Laboratory, Los Alamos, NM, USA
[e] NASA Johnson Space Centre, Houston, TX, USA
[f] Natural History Museum of Denmark, University of Copenhagen, Copenhagen, Denmark

Received 30 May 2018; accepted in revised form 21 November 2018; available online 27 November 2018

Abstract

The Mars Science Laboratory's Chemistry and Camera (ChemCam) instrument suite on-board the *Curiosity* rover has analysed ~1200 sedimentary targets during the mission up to sol 1482. These targets have included sedimentary rock, diagenetic features (e.g., fracture-associated alteration halos, mineral veins, nodules, and erosion resistant raised ridges), active aeolian fines, soils and float. We have isolated ChemCam geochemical trends relating to diagenetic features and alteration products from those of the sedimentary rock in order to identify the compositional characteristics of Gale crater's sediment source regions. The effects of grain size variation on sedimentary unit geochemistry have been taken into account by grouping and analysing geological units according to grain size. With obvious diagenetic features removed from the database, and predominately isochemical aqueous alteration inferred for the Mt Sharp Group samples, we propose that source region composition is a stronger source of geochemical change between the Bradbury and Mt Sharp Groups than open-system alteration. Additionally, a lack of correlation between the Chemical Index of Alteration (CIA) values and SiO_2, MgO or FeO_T indicates that the slight increase in chemical weathering of the Mt Sharp Group sediments was insufficient to overprint sediment source compositional signatures. This has led to the identification of five unique igneous endmember compositions which we hypothesise to have contributed to Gale crater's stratigraphic record. These endmembers are: (1) a subalkaline basalt, compositionally similar to the tholeiitic Adirondack Class basalts of Gusev crater, and dominant within the finer grained units up to the base of Mt Sharp; (2) a trachybasalt, mostly identified within conglomerate units from the Darwin waypoint to the base of Mt Sharp; (3) a potassium-rich volcanic source, determined from strong potassium enrichment and a high abundance of sanidine that is most dominant in the fluvial sandstones and conglomerates of the Kimberley formation; (4) a highly evolved, silica-rich igneous source that correlates with the presence of tridymite, and is recorded in the lacustrine mudstone of Mt Sharp's Marias Pass locality; and, (5) a fractionated, relatively SiO_2-rich subalkaline basalt, seen to have influenced the composition of mudstone deposited in the lower part of the Mt Sharp Group. Endmembers (1), (2), (3), and (4) have previously been identified at specific waypoints along the rover's traverse, but we show that their influence extends throughout Gale's stratigraphic record. The occurrence of detected endmembers is also strongly correlated with stratigraphic position, which suggests changing

* Corresponding author.
E-mail addresses: Candice.bedford@open.ac.uk (C.C. Bedford), j.bridges@leicester.ac.uk (J.C. Bridges), Susanne.schwenzer@open.ac.uk (S.P. Schwenzer), rwiens@lanl.gov (R.C. Wiens), Elizabeth.b.rampe@nasa.gov (E.B. Rampe), jfrydenvang@snm.ku.dk (J. Frydenvang), gasda@lanl.gov (P.J. Gasda).

https://doi.org/10.1016/j.gca.2018.11.031
0016-7037/

sediment source regions with time. We conclude that Gale sediment provenances were much more varied than suggested by the largely homogenous, globally-distributed Martian basalt inferred from orbit, showing that complex magmatic assemblages exist within the ancient highland crust surrounding Gale.

Keywords: Mars; Gale crater; LIBS; Diagenesis; Source regions; Chemical weathering; MSL; Curiosity

1. INTRODUCTION

Mars' global sedimentary record has been generated by fluvial, lacustrine, glacial, and aeolian processes (e.g., Malin and Edgett, 2000; Hynek and Phillips, 2001; 2003; Stack et al., 2014a). Throughout geological time, these processes have eroded sediments from their source rocks in the Martian crust, and redeposited them elsewhere as sedimentary units. Understanding the origin of these sediments can potentially provide information on Mars' crustal compositions, and the igneous processes that generated them (e.g., McSween et al., 2009; Mangold et al., 2017b). Orbital mapping with Mars Global Surveyor and Mars Odyssey data has shown that the mineralogy of Mars' surface is dominated by primary mafic igneous minerals such as olivine and pyroxene (Bandfield et al., 2000; Hamilton and Christensen, 2005; Chevrier and Mathé, 2007; Hanna et al., 2016). This predominance of primary mafic minerals on the planet's surface suggests that a relatively low rate of chemical weathering has been present throughout Mars' geological history, and indicates that Mars' crust is chiefly basaltic in composition (McSween et al., 2009). However, some occurrences of silica-rich and alkali-rich material have been observed in Martian samples such as in Martian meteorites NWA 6963 (Filiberto et al., 2014), NWA 7034 (Agee et al., 2013) and NWA 7533 (Humayun et al., 2013). Orbital data have also detected silica-rich material on the NW flank of Syrtis Major (Bandfield et al., 2004), though it is debated whether this relates to evolved crustal material (Bandfield et al., 2004; Bandfield, 2006) or late-stage aqueous alteration (Smith and Bandfield, 2012). Silica-rich and alkali-rich igneous float and sediments have been identified at the surface in Gale crater (Sautter et al., 2014; 2015; Morris et al., 2016; Edwards et al., 2017) and show that evolved magmatic compositions could be more widespread on Mars than that which is indicated by Near Infrared spectroscopy from orbit. Several factors have impeded the remote detection of these evolved compositions on the surface, for instance; hydrothermal alteration of the Martian crust (Bibring et al., 2006; Ehlmann et al., 2013), global dust which obscures much of the planet (McSween et al., 2009), and widespread, mixed Martian basaltic soil identified from ground-based observations (Chevrier and Mathé, 2007). Hence, identifying evolved crustal compositions requires landed missions such as the NASA *Pathfinder*, Mars Exploration Rovers (MER), and Mars Science Laboratory (MSL).

Since landing in August 2012, MSL has been geochemically and mineralogically analysing the sedimentary succession within Gale crater along its >19.6 km drive to date (Fig. 1). The Early Hesperian-age Gale crater was selected as the MSL landing site due to its low elevation as a closed basin, and the ~5 km high, stratified sedimentary mound *Aeolis Mons*, informally named "Mt Sharp", which was seen from orbit to have hydrated clay- and sulfate-bearing units (Milliken et al., 2010; Fraeman et al., 2016) on its lower slopes. These hydrated units made Gale a good candidate site to better understand the role water played in Mars' early history, and to determine whether Gale crater was habitable at some point in its past (Grotzinger et al., 2014). A key MSL mission objective is to analyse the geology and geochemistry of this preserved geological record in order to assess paleoenvironmental change in relation to the depositional environments of the sedimentary units (Grotzinger et al., 2012). The paleo-environment of deposition is not the only contributor to sediment geochemistry; source region composition and the weathering conditions of the sediment host rock are also key components (Weltje, 2012). In addition to its primary mission aim, the MSL's campaign therefore presents a unique opportunity to investigate Martian source region characteristics recorded in the sediments using the extensive geochemical dataset acquired by its instruments with, in particular for our study, ChemCam (Laser-Induced Breakdown Spectroscopy) and CheMin (X-ray Diffraction). The ChemCam instrument aboard MSL analysed ~1200 sedimentary targets within the period of the study (up to sol 1482), generating the most in-depth Martian chemostratigraphic record to date on another planet.

Terrestrial provenance studies have shown that the mineralogy and geochemistry of fine-grained clastic sedimentary units are largely characteristic of their source region, provided the extent of aqueous alteration, transport fractionation, and the effects of grain size variation have been taken into account (Nesbitt and Young, 1982; Roser and Korsch, 1986; Herron, 1988; Nesbitt and Wilson, 1992; Kroonenberg, 1994; Jin et al., 2006; Tolosana-Delgado and von Eynatten, 2009; Bloemsma et al., 2012; Weltje, 2012). Many terrestrial studies utilised ratios of major element oxides such as SiO_2/Al_2O_3 and Na_2O/K_2O (e.g., Pettijohn et al., 1972; Roser and Korsch, 1986; Jin et al., 2006) to classify sediments according to magmatic source regions (Roser and Korsch, 1986; Herron, 1988; Kroonenberg, 1994), or determine the extent of chemical weathering they have undergone (Nesbitt and Young, 1982; Nesbitt and Wilson, 1992; Babechuk et al., 2014). If the mineralogical differences are acknowledged between the Earth and Mars (i.e., quartz is abundant in Earth's sedimentary record and not in that of Mars), these terrestrial methods for determining sediment source region variations have the potential to be applied to ChemCam instrument major element compositions of sedimentary targets. Therefore, in this study we have grouped ChemCam major element analyses according to stratigraphic position, grain

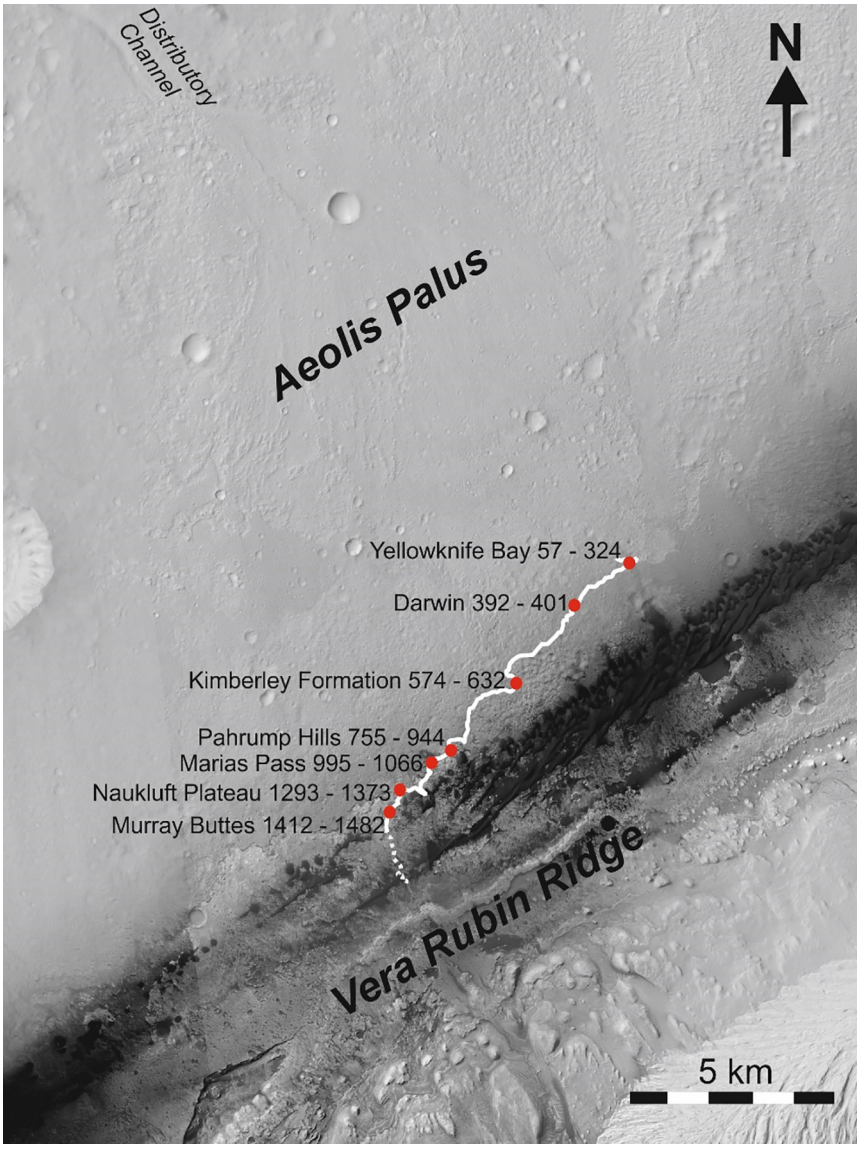

Fig. 1. Annotated HiRISE map (Calef III and Parker, 2016) of NW Gale crater showing the rover traverse (white line) up to sol 1482 with key waypoints and associated sol numbers labelled as red dots. (For interpretation of the references to colour in this figure legend, the reader is referred to the web version of this article.)

size, and target textural characteristics, to distinguish the extent of post-depositional aqueous alteration on our samples, and delineate the effects of grain size on geochemistry. Then, we have utilised the mineralogical data provided by the Chemistry and Mineralogy (CheMin) instrument alongside the ChemCam dataset to gain some understanding of the compositional diversity of the Martian crust in the source regions around Gale.

1.1. Gale crater's sedimentary record

The Gale crater succession encountered by MSL consists of mudstone-, fine to coarse sandstone-, and conglomerate-rich units. These units were interpreted to have been deposited in a dominantly fluviolacustrine paleoenvironment (Grotzinger et al., 2014; Grotzinger et al., 2015) following the formation of the crater $\sim 3.8 \pm 0.3$ Ga (Thomson et al., 2011). Stratigraphic analysis showed that sediments infilled the crater and were subsequently exhumed and eroded by aeolian processes, leaving the present day $\sim$5 km high, stratified Mt. Sharp (Grotzinger et al., 2015).

Stratigraphic subdivisions of Gale crater along the rover traverse (Figs. 2, 3) are:

- The Bradbury Group, consisting of mostly fluvially-deposited conglomerate and sandstone, associated with deposition during delta progradation and sampled by the rover during sols 1–750 (Grotzinger et al., 2015).

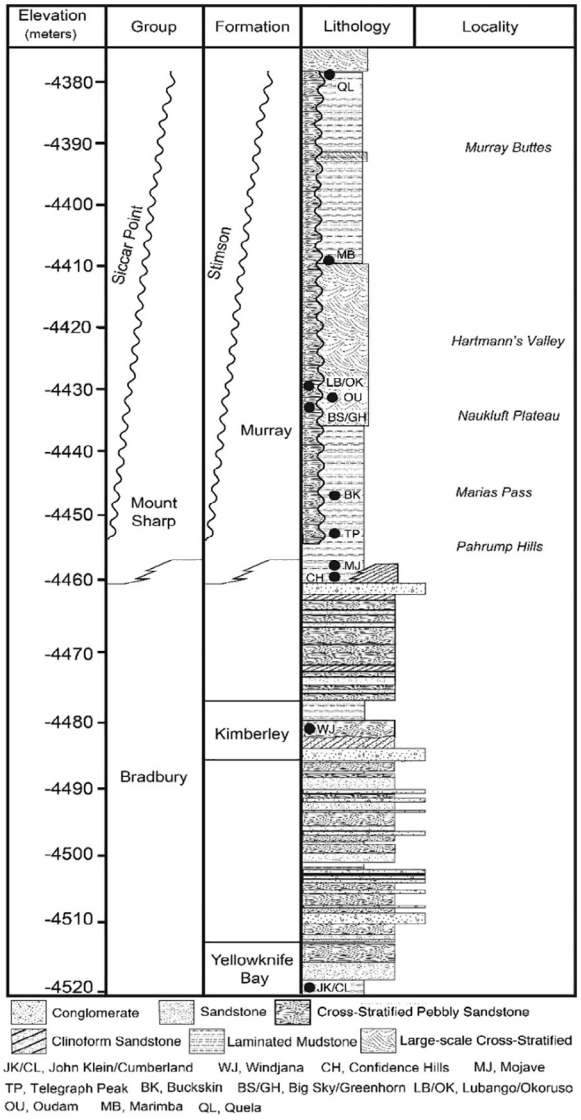

Fig. 2. A stratigraphic column detailing the morphological characteristics of each stratigraphic group and unit encountered by MSL up to the Murray Buttes waypoint. Drill hole locations are denoted by a black dot. Image credit: The MSL sedimentology and stratigraphy working group.

- The Mt. Sharp Group (analysed from sol 755; Fig. 1), largely composed of finely-laminated mudstone (Murray Formation), deposited within the standing water body located at the end of Gale's ancient fluviolacustrine system (Grotzinger et al., 2014, 2015; Stack et al., 2016).
- The Siccar Point Group (which constitutes the Stimson Formation, and was analysed by ChemCam during sols 990–1352), a lithified aeolian capping unit that unconformably overlies the Mt. Sharp Group (Fraeman et al., 2016; Banham et al., 2018).

In this study, we have solely analysed the data collected from the Bradbury and Mt Sharp stratigraphic groups in order to focus our geochemical interpretation on sediments deposited in the fluviolacustrine setting, as well as to examine the composition of the most ancient sedimentary units so far analysed by MSL within Gale crater.

This study aims to expand upon the key areas of geochemical interest within the Bradbury (Yellowknife Bay formation, Darwin waypoint, Kimberley formation) and Mt Sharp Groups (Pahrump Hills, Marias Pass, and Murray Buttes localities) that have provided a basis for previous studies into sediment source regions (McLennan et al., 2014; Vaniman et al., 2014; Anderson et al., 2015; Sautter et al., 2015; Mangold et al., 2015; Le Deit et al., 2016; Mangold et al., 2016; Morris et al., 2016; Thompson et al., 2016; Treiman et al., 2016; Edwards et al., 2017; Hurowitz et al., 2017; Mangold et al., 2017b; Rampe et al., 2017a; Siebach et al., 2017). These studies show the sediments to be largely basaltic in nature, though alkali- and silica-enrichments have also been identified in Gale's sediments, possibly relating to distinct, evolved magmatic source regions (Le Deit et al., 2016; Morris et al., 2016; Thompson et al., 2016; Treiman et al., 2016; Siebach et al., 2017). MSL has also identified evidence for fractionated crustal compositions in over 60 ChemCam targets of float and conglomerate clasts that show clear textural evidence – porphyritic, cumulate or vesicular – for an igneous origin (Sautter et al., 2014; Mangold et al., 2016; Cousin et al., 2017; Edwards et al., 2017). Their compositions ranged from basalt (most abundant) to trachybasalts (Edwards et al., 2017).

1.1.1. The Bradbury Group

Three key waypoints were analysed by MSL within the Bradbury Group: Yellowknife Bay, Darwin and Kimberley. Yellowknife Bay (sols 57–324) consists of a 4–6 m thick lacustrine mudstone (Sheepbed Member) overlain by cross-bedded, fluvial sandstone and conglomerate (Gillespie Lake and Glenelg Members; Figs. 2 and 3B). Widespread diagenetic features – which will be discussed in more detail in Section 1.2 – were identified in the sedimentary succession at this waypoint, such as raised ridges (Leveille et al., 2014; Fig. 4A), filled and hollow nodules (Stack et al., 2014b; Fig. 4B), and sulfate veins (Rapin et al., 2016; Fig. 4C). Two samples (John Klein and Cumberland) were drilled from the Sheepbed mudstone and delivered to CheMin for mineralogical analysis (Vaniman et al., 2014).

After Yellowknife Bay, MSL arrived at the Darwin outcrop (sols 392–401) which is comprised of multiple exposures of conglomerate and sandstone bedrock, overlain by sand drifts and dark float accumulations (Vasavada et al., 2014; Mangold et al., 2016). Exposures of these conglomerates were also identified on the traverse leading up to and beyond the Kimberley formation described below (Mangold et al., 2016). Several clasts of igneous rock were identified at this locality within conglomerate units, or as igneous float (Mangold et al., 2016; Cousin et al., 2017; Edwards et al., 2017). These have been used as a comparison dataset in our study.

The final key waypoint investigated by MSL in the Bradbury Group is the Kimberley formation (sols 574–632). The Kimberley formation is the stratigraphically youngest key waypoint of the Bradbury Group (Grotzinger et al., 2015), and constitutes a fining upwards

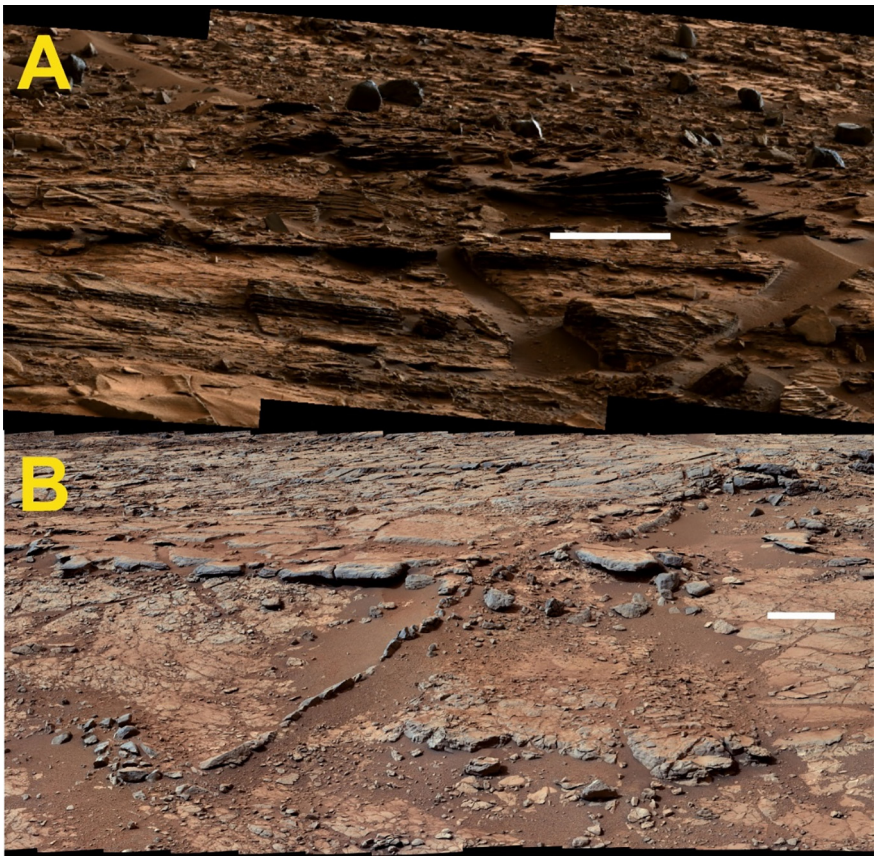

Fig. 3. Mastcam images of the two fluviolacustrine stratigraphic groups. (A) The Murray Formation (Mt Sharp Group), which consists of laminated mudstones with some interstratified fine-sandstones (Chinle Peak, ML_mcam03617, sol 821). (B) The Yellowknife Bay formation (Bradbury Group), with Sheepbed member mudstones capped by Gillespie Lake member sandstones and conglomerates (ML_mcam00817, sol 137). Scale bar measures 50 cm.

sequence of polymict conglomerate to fine to medium-grained sandstone, capped by a massive coarse sandstone member (Thompson et al., 2016; Treiman et al., 2016). This formation was subdivided into the Point Coulomb and Liga conglomerate, Square Top fluvial sandstone, Dillinger trough cross-bedded sandstone, and Mt. Remarkable massive sandstone Members. These Members were analysed by ChemCam and the Alpha Particle X-Ray Spectrometer (APXS) instrument (Grotzinger et al., 2015; Le Deit et al., 2016; Thompson et al., 2016), and the Windjana sample was drilled from the Dillinger Member and delivered to CheMin (Treiman et al., 2016).

1.1.2. The Mt Sharp Group (Murray formation)

The lower Murray formation (lowermost unit of the Mt. Sharp Group from the Pahrump Hills to Marias Pass locality; Figs. 1–3A) is a laminated, fine-grained mudstone that appears stratigraphically ~20 m above the Kimberley formation (Fig. 2; Grotzinger et al., 2015). Drilled samples from the lower Murray formation Pahrump Hills include Confidence Hills, Mojave 2, and Telegraph Peak (Rampe et al., 2017a), along with Buckskin from Marias Pass (Morris et al., 2016). The change from the Bradbury Group to the Mt. Sharp Group was marked by a transition from fluvial sandstone and conglomerate, detected at the base (e.g., Bald Mountain, sols 775–778), to thinly laminated mudstone with extensive diagenetic features such as erosion resistant nodules, raised ridges, and dark and light mineral veins (Nachon et al., 2017). Cross-laminated mudstone/siltstone and fine-grained sandstone facies are also present in this unit, but overall grain size varies much less than in the Bradbury Group (Grotzinger et al., 2015; Hurowitz et al., 2017; Rampe et al., 2017a; Siebach et al., 2017).

From orbit, the Murray Formation appears homogeneous, at least up to the Vera Rubin (Hematite) Ridge, and has intermittent areas with notable infrared signatures from orbit of phyllosilicate and sulfate (Fraeman et al., 2013, 2016). From rover observations, a distinction can be made within the Murray formation between Murray units containing abundant hematite, and Murray units with high abundances of magnetite and crystalline silica (Morris et al., 2016; Hurowitz et al., 2017; Rampe et al., 2017a). The apparent interfingering boundary between Bradbury Group sediments and the Murray formation implies coeval deposition as the rivers transporting material from the crater rim reached a perennial lake (Grotzinger et al., 2015). Moving up the Mt. Sharp stratigraphic succession towards the Murray Buttes, the Murray formation was seen to be punctuated by a section of trough cross-bedded, fine-grained sandstone and siltstone, followed by a return to well-

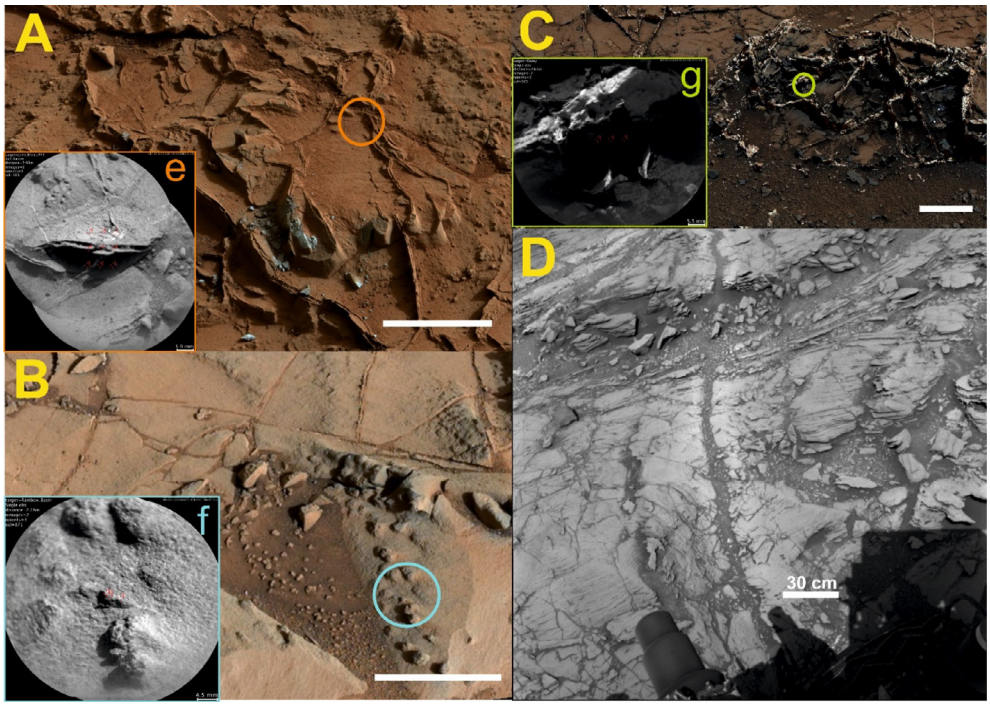

Fig. 4. Mastcam, Navcam and RMI examples of identified alteration targets (A) Raised ridge target John Klein RP3 (sol 165) in the Bradbury Group Sheepbed Member, (B) Nodule target Rainbow Basin (sol 871) in the Mt Sharp Group Pahrump Hills locality, (C) vein target Ouray (sol 929) in the Mt Sharp Group Garden City locality, and (D) Alteration halo target Whitewater (sol 1094) at the Mt Sharp group, Marias Pass waypoint. MastCam, RMI and MAHLI (NASA/JPL-Caltech/MSSS). Scale bar measures 10 cm, except for D which measures 30 cm. Images (e–g) are the RMI mosaics for the respective alteration feature footprints highlighted by the circles.

laminated mudstone, with some interstratified sandstone. CheMin samples were drilled from the Murray formation encountered after the Naukluft plateau (sols 1373–1482) are Oudam and Marimba 2 (Bristow et al., 2017; Rampe et al., 2017b).

1.2. Aqueous alteration within Gale crater sediments

The variety of alteration features seen within the Gale crater stratigraphy – especially in the mudstone members – suggests that aqueous alteration occurred after deposition and lithification of the sediments (Leveille et al., 2014; Nachon et al., 2014; Bridges et al., 2015; Rapin et al., 2016; Schwenzer et al., 2016; Frydenvang et al., 2017; Nachon et al., 2017). Some features were identified throughout the stratigraphic record, such as calcium-sulfate mineral veins (Nachon et al., 2014; Rapin et al., 2016; L'Haridon et al., 2018). Meanwhile others were seen in specific areas (Fig. 4) i.e., raised ridges in Yellowknife Bay (Leveille et al., 2014), Mg-rich dendritic concretions at Pahrump Hills (Kah et al., 2015), dark mineral veins at Garden City (Nachon et al., 2017; L'Haridon et al., 2018), and alteration halos between Marias Pass and Bridger Basin (Frydenvang et al., 2017; Yen et al., 2017).

ChemCam analyses taken across diagenetic features show that chemical remobilisation appears localised to weaknesses in the lithological units such as fractures (Frydenvang et al., 2017; Nachon et al., 2017; L'Haridon et al., 2018). These weaknesses were exploited by the groundwater causing the dissolution and precipitation of soluble minerals and mobile elements along them. Hence, the low permeability of the units appears to have limited the open system alteration in bulk rock compositions away from the structural weaknesses of the bedrock (McLennan et al., 2014; Anderson et al., 2015).

In addition to the obvious diagenetic features, so far all Gale crater CheMin analyses of host rock and soil targets have contained a substantial proportion (16–60 wt%) of an amorphous and phyllosilicate (AP) component (Bish et al., 2013; Blake et al., 2013; Dehouck et al., 2014; Vaniman et al., 2014; Treiman et al., 2016; Rampe et al., 2017a). A best estimate of the AP abundance and composition can be modelled using a full-pattern FULLPAT fitting method which compares known terrestrial natural and synthetic amorphous and clay samples to Mars CheMin analyses (Chipera and Bish, 2002, 2013). Then AP compositions are calculated through a mass balance calculation using the bulk sample geochemistry analysed by the APXS instrument combined with the modelled FULLPAT sample phase abundances (Morrison et al., 2018). The amorphous component in the lithified sedimentary units – whether basaltic or silicic – has largely been hypothesised to relate to diagenetic cement derived from the aqueous alteration of the volcanic minerals or glass that constitute Gale's sedimentary units (Vaniman et al., 2014; Treiman et al., 2016; Rampe et al., 2017a). In general, the calculated chemical composition of the AP component has been associated with material initially derived from a basaltic source (Bish et al., 2013; Blake et al., 2013; Dehouck et al., 2014; Vaniman et al., 2014), except for the high-silica amorphous

component in the Buckskin drill hole that was instead associated with an evolved volcanic source and/or enhanced leaching (Morris et al., 2016; Frydenvang et al., 2017).

In this study we will first characterise the extent of the geochemical remobilisation associated with the observed aqueous alteration features and calculated AP components up to sol 1482. If bulk rock geochemical compositions are shown to be uncorrelated with Gale crater alteration trends, sediment source characteristics can be identified. As the AP component may relate to diagenesis, and as it constitutes a substantial proportion of Gale's sedimentary targets, it is crucial to understand the geochemical effect of the amorphous component on ChemCam analyses. Thus, we have also compared the CheMin and APXS derived compositions of the AP components to the bulk host rock geochemistry. If the compositions are similar between the AP component and local host rock, the AP component can be identified as a product of closed system chemical weathering, and sediment source characteristics can be constrained.

2. METHODS

2.1. ChemCam instrument

The remote sensing Chemistry and Camera (ChemCam) instrument suite uses a Laser-Induced Breakdown Spectroscopy (LIBS) instrument to ablate a target host rock or soil in order to acquire its major, minor and trace element compositions (Maurice et al., 2012; Wiens et al., 2012; Clegg et al., 2017). A series of 14 mJ laser pulses is directed at a target between 2.2–7.0 m from the rover mast to induce a short-lived plasma on the incident sample (Maurice et al., 2012; Wiens et al., 2012; Maurice et al., 2016). The excited electrons of the atoms and ions within the sample then emit at diagnostic wavelengths as they decay to lower energy levels, which are subsequently detected by the telescopic imager and passed to three spectrometers in the 240–340 nm ultra-violet light (UV), 380–470 nm violet (VIO), and 470–900 nm visible and near infra-red (VNIR) spectral ranges (Wiens et al., 2012).

Each target is analysed by a raster pattern of observation points which in turn consist of 30–50 spectral analyses. The repeated firing of the laser at a specific point on the incident target removes dust in the first five laser pulses with further pulses generating a sample depth profile (Wiens et al., 2012). Observation point analyses are averages of the spectra conducted at a given raster point. Raster geometries occur in either a matrix (2×2, 3×3, 4×4, or 5×5), or a linear (5×1, 10×1, or 20×1) configuration. Point footprints range from 350–750 μm in size depending on distance from the rover (Wiens et al., 2012; Maurice et al., 2016). This small footprint enables the identification and analysis of small-scale features such as diagenetic mineral veins and clasts, which make it imperative that the context of each analysis is documented. As such, the ChemCam baseline analysis sequence collects Remote Micro Imager (RMI) images with a submillimetre resolution of ~90 μrad before and after the LIBS analysis (Maurice et al., 2012; Le Mouélic et al., 2015), which have been used in this study for target classification alongside the rover's other on-board cameras Mast Camera (Mastcam) (Malin et al., 2017) and Mars Hand Lens Imager (MAHLI) (Edgett et al., 2012).

Quantitative analysis is achieved for each observation point by processing the LIBS spectra through several preprocessing steps to yield clean atomic emission spectra (Wiens et al., 2013). The spectra averaged from all the laser shots minus the first five (to remove the effects of surface dust) is then calibrated against a set of more than 400 standards, including on-board calibration targets (Vaniman et al., 2012; Blaney et al., 2014) in a process that combines sub-model Partial Least Squares regression (PLS) (Anderson et al., 2017) and an Independent Component Analysis (ICA) algorithm (Clegg et al., 2017). This yields the abundances of eight major elements (SiO_2, TiO_2, Al_2O_3, FeO_{total}, MgO, CaO, Na_2O, and K_2O) in the form of oxide wt%. Accuracy and precision for each element oxide are noted in Table A.1 of Appendix A. In our study, the totals were not normalized to 100 % to account for any non-determined contributions of S, P, F, Cl, and H, which ChemCam does not routinely analyse.

Mean accuracies for the observation points presented here are given in Table A.1 of Appendix A, and are used for comparison with absolute abundance values, such as mineral compositions, or for comparisons with measurements made by other instruments. ChemCam instrument precision corresponds to the error presented with APXS results (Blaney et al., 2014). It is used to compare different ChemCam observations. The ChemCam LIBS precision is significantly less than the standard deviations of the mean compositions of the various units discussed here (Blaney et al., 2014). In addition to the geochemical data from the ChemCam instrument, we also use Gale crater mineralogical data derived by the Chemistry and Mineralogy instrument suite (CheMin). CheMin data was acquired from the NASA Planetary Data System (PDS) and peer-reviewed articles (Vaniman et al., 2014; Morris et al., 2016; Treiman et al., 2016; Rampe et al., 2017a; Morrison et al., 2018) to provide complementary mineralogical data to the ChemCam major element data.

2.2. Statistical approach to ChemCam data

This study encompasses sols 1–1482 of the MSL mission. Within this period the ChemCam instrument analysed almost 1200 targets, and close to 9500 observation points. Due to the small sampling footprint, 350–750 μm (Maurice et al., 2016), on targets of varying grain size and heterogeneity, target analyses for coarse-grained lithologies (>1 mm) were often not representative of whole-rock geochemistry. To counter this effect, we analysed the dataset in its entirety through compositional trends displayed on a series of scatter and density contour plots, in addition to simple and multiple linear regression models. The scatter plots highlight any compositional trends between two major element oxides. The density contour plots are essentially histograms in two dimensions which show the major element distribution as isolines (contours) of x and y. The two-dimensional histograms are smoothed according to the methods of Eilers and Goeman (2004). The smoothing factor used in this study is 20. After smoothing of the

two-dimensional histograms, the contours are generated, and are representative of the proportion of data point density within each smoothed 'pixel' of a 100 × 100 grid. Density contour plots show the compositional spread of the data population and can be used with histograms to highlight compositional foci and geochemical trends across stratigraphic units (Edwards et al., 2017). For our ChemCam dataset of the sedimentary rock record, the density contour plots have the added benefit of indicating bulk rock compositions as they are not as easily affected by outlying compositions from individual minerals or alteration features that could skew the mean (see Appendix A.1 for an example).

Major element oxide Simple Linear Regression (SLR) models (Neter et al., 1996) were determined for the Bradbury and Mt Sharp stratigraphic groups (see Appendix B) using Minitab v17. Statistically significant major element correlations for the dataset were calculated using Pearson's correlation coefficients (r) for each plotted major element oxide, which were then compared to the p-value of their associated student's t-test statistic. The t-test statistics and p-values were calculated for a significance level $\alpha = 0.05$ based on the null hypothesis that there is no correlation between the two major element variables (H_0: $\rho = 0$). Appendix B shows tables of each major element oxide's relative r and p-values for each of the stratigraphic groups.

As an increase in the proportion of Al_2O_3 to CaO, Na_2O, K_2O, MgO, and FeO_T has been associated with greater sediment chemical weathering and aqueous alteration (Nesbitt and Young, 1982; Nesbitt and Wilson, 1992; McLennan et al., 2014; McLennan et al., 2015; Hurowitz et al., 2017); a Multiple Linear Regression (MLR) model (Neter et al., 1996) was constructed to show the variation in Al_2O_3 as a response to predictors SiO_2, TiO_2, FeO_T, MgO, CaO, Na_2O, and K_2O. This can statistically distinguish which major elements contribute the most to aluminium's variation, and help ascertain whether or not this is indeed related to chemical weathering regimes, or source region characteristics. The statistical significance of how the predictor variables contribute to the variation in Al_2O_3 is shown via the p-value calculated using the student's t-test statistic. Similar to the SLR models outlined above, the model is built around the null hypothesis that there is no fit between the response and predictors (H_0: $\rho = 0$). The results and residual plots are shown in Appendix B. Residual plots (probability and order) are also given in the appendix to illustrate the data statistics. When discussing the initial major element correlations within the dataset, Pearson's correlation coefficients are used to show the strength of the major element correlation (assuming it is linear) and whether the correlation in question is positive or negative. R^2 values are provided in the SLR and MLR model outputs (Appendix B) and are also given to show the fit of the models to the dataset.

2.3. Removing the effects of alteration from the bulk rock dataset

ChemCam has observed a variety of geological targets (i.e., soils, mineral veins, sandstone, igneous float). As our study focuses on source region inferences from lithified sedimentary units, we grouped ChemCam observation points based on Mastcam, Navcam, MAHLI, and RMI images into the "constrained bulk rock", "alteration", "unconsolidated sediment", and "float" datasets (Fig. A.2). The constrained bulk rock dataset consists of ChemCam observations that targeted sedimentary outcrop away from obvious aqueous alteration features. We further refined the constrained bulk rock dataset by removing observation points with total sum of oxides outside the range considered acceptable for the purpose of this study, 95–105%. This minimised and effectively removed any sediments associated with high quantities of S and H, volatiles which are not included in standard ChemCam analyses. Restricting the constrained bulk rock dataset to 95–105% total sum of oxides also helps isolate and remove geochemical trends relating to sulfate salts. In order to discuss how source region compositions varied relative to geological time, the constrained bulk rock dataset has been subdivided into the main stratigraphic groups (Bradbury and Mt Sharp), as well as the key waypoints discussed in Section 1.1 where MSL conducted detailed investigations into the surrounding bedrock (see Section 2.5 for more details).

In order to minimise the influence of post-depositional alteration on the constrained bulk rock geochemistry, any LIBS pit observed to overlap a diagenetic feature in RMI images was removed from the main dataset and grouped separately. The "alteration feature dataset" consists of LIBS points that have sampled the many aqueous alteration features identified in the Bradbury and Mt Sharp stratigraphic Groups that formed through the interaction of groundwater and rock (see Section 1.2 and Fig. 4). We carefully documented all those targets, which on the basis of their morphology were of secondary (diagenetic) origin, e.g., raised ridges, nodules, veins. As the alteration feature dataset investigates the geochemical trends of alteration (including concentration of S and H, among other elements not tracked quantitatively by ChemCam) on Gale crater host rock, we do not restrict alteration feature LIBS analyses to the 95–105% total range that we placed on the constrained bulk rock dataset. This alteration feature dataset was then compared to that of the constrained bulk rock dataset in order to assess the extent that these aqueous alteration processes may have affected our estimates of the pre-alteration bulk rock geochemistry.

Observation points taken at the Marias Pass locality may demonstrate silica enrichment associated with diagenesis, as well as detrital tridymite and cristobalite (Morris et al., 2016; Frydenvang et al., 2017). To minimise the influence of alteration in Marias Pass host rock targets we only included ChemCam observation points taken at the Lion Outcrop where the Buckskin drill hole was conducted and where tridymite was detected (Morris et al., 2016). Tridymite only forms in high-temperature, low pressure conditions, and so was assumed to relate to an igneous protolith and not alteration, although subsequent alteration could have led to the formation of opaline silica detected in the Buckskin target (Morris et al., 2016). As diagenetic halos and associated silica-enrichment were usually accompanied by a strong

light-toned colour change in the bedrock (Frydenvang et al., 2017), light-toned targets in this area were assumed to mark altered bedrock and have been excluded.

Observation points identified in RMI images to show soil contamination were removed along with targets disturbed by the rover (e.g., drill cuttings and dump piles formed as a product of drilling and CheMin analysis). Non-igneous float and pebbles were identified based on the presence of sedimentary features (such as laminations and cross-bedding) or a lack of convincing igneous textures (i.e., porphyritic, vitreous, vesicular) and were excluded from the results presented here. Finally, we also removed all igneous clasts and float from the refined dataset and placed them into a comparison dataset.

2.4. Categorising the constrained bulk rock dataset according to grain size

Terrestrial sediment compositions have been shown to strongly correlate with grain size due to the processes that generate the sediments from crystalline rocks (i.e., chemical and physical weathering) (Pettijohn, 1954; Bloemsma et al., 2012; Weltje, 2012; Siebach et al., 2017). Therefore, in order to separate sedimentary processes from source rock endmember compositions, it is necessary to group and discuss samples according to grain size dependent subpopulations (Weltje, 2012). Average grain sizes of the analysed geological units and key waypoints were obtained from literature studies which used MAHLI, RMI and Mastcam images (Meslin et al., 2013; Grotzinger et al., 2014; Anderson et al., 2015; Grotzinger et al., 2015; Mangold et al., 2016; Treiman et al., 2016; Siebach et al., 2017; Mangold et al., 2017b). Average grain sizes are used as grain size determination is dependent on a well-focused image taken of a relatively dust free target which is not always possible (Mangold et al., 2017b).

Coarse-grained units were defined as those with resolvable grain sizes greater than 1 mm (Mangold et al., 2016; Mangold et al., 2017b) and were usually seen in the Bradbury Group to typically consist of clast-supported conglomerates. These were poorly sorted, with sub-rounded to sub-angular pebbles. Sand grains (defined as 0.062–1 mm) can be resolved with RMI and MAHLI images but are only identifiable using Mastcam if larger than 0.15 mm (Mangold et al., 2017b). The minimum grain size that MSL cameras can identify requires a resolution of at least 3 pixels (Mangold et al., 2017b). Therefore, at the optimum MAHLI working distance (~2 cm), grains finer than very fine sand (<0.062 mm) are largely unresolvable and constitute the mudstone grain size category (Mangold et al., 2017b). Average grain sizes for each stratigraphic group and unit are provided in Fig. A.2. of Appendix A.

2.5. Categorising the constrained bulk rock dataset according to stratigraphic position

The constrained ChemCam bulk rock database was divided into stratigraphic subgroups to help ascertain any change in endmember source compositions. The stratigraphic group divisions (Bradbury and Mt. Sharp up to sol 1482) were used to study the geochemical variation between distinct paleoenvironmental settings. A more detailed study into the compositional variation within stratigraphic groups was then provided with the analysis of stratigraphic units and waypoints, such as those outlined in Section 1.1. Fig. A.2. of Appendix illustrates each of the subgroup divisions used in our study and Table A.2 provides the total number of observation points included for each stratigraphic unit and area.

3. RESULTS

In this section, we discuss the geochemistry of the constrained bulk rock dataset (Section 3.1) followed by the geochemical trends identified in the alteration dataset (Section 3.2). Overall, the Bradbury and Mt. Sharp (Murray formation to sol 1482) stratigraphic groups exhibit distinct geochemical foci and trends across the major element oxide compositions of the ChemCam observation points (Figs. 5, 6). The constrained bulk rock dataset – subdivided according to stratigraphic group – are plotted in Fig. 5 as frequency histograms and as a series of Harker density contour plots in Figs. 6–8. Basic statistics for the constrained Bradbury and Mt Sharp bulk rock datasets are provided in Table 1. Alteration targets (ridges, veins, etc.), calculated amorphous and phyllosilicate (AP) components, and CheMin modelled primary igneous mineral phases are plotted alongside the constrained stratigraphic group density contours in Figs. 7 and 8. The CheMin AP compositions are shown in Figs. 7 and 8 to help discern the influence these components have on the modelled constrained bulk rock geochemistry. Compositions of the AP components for various drilled samples were calculated by Vaniman et al. (2014), Treiman et al. (2016), Morris et al. (2016), Rampe et al. (2017a), and Morrison et al. (2018) based on CheMin abundances and APXS-derived compositions (see Section 1.2 for details on how the AP compositions are derived).

3.1. Major element variation and correlation within the stratigraphic groups

The Bradbury Group demonstrates a clear bimodality in its histograms for MgO, Na_2O, and Al_2O_3 (Fig. 5). Peak MgO compositions occur at 0.8–1.3 and 7.1–7.6 wt%; Na_2O peaks occur at 2.9–3.1 and 5.2–5.4 wt%; and Al_2O_3 peaks occur at 10.4–11.0 and 17.8–18.3 wt%. The Bradbury Group shows a unimodal distribution in the histograms for SiO_2, TiO_2, FeO_T, CaO, and K_2O (Fig. 5). These unimodal distributions are generally asymmetric, with the exception of CaO that is symmetrical (Fig. 5). This asymmetry is particularly apparent for K_2O which is strongly left skewed, SiO_2 and TiO_2 that are weakly left skewed, and FeO_T which is weakly right skewed, suggesting an influence by extreme outliers on the mean compositions (Figs. 5, 6). Density contours of the Bradbury Group are generally present as concentric circles about the mean (Fig. 6), but with a slight deviation for the outermost edges towards higher Al_2O_3, FeO_T, Na_2O, and K_2O, and lower FeO_T, MgO, and Na_2O concentrations (Fig. 6). These deviations roughly

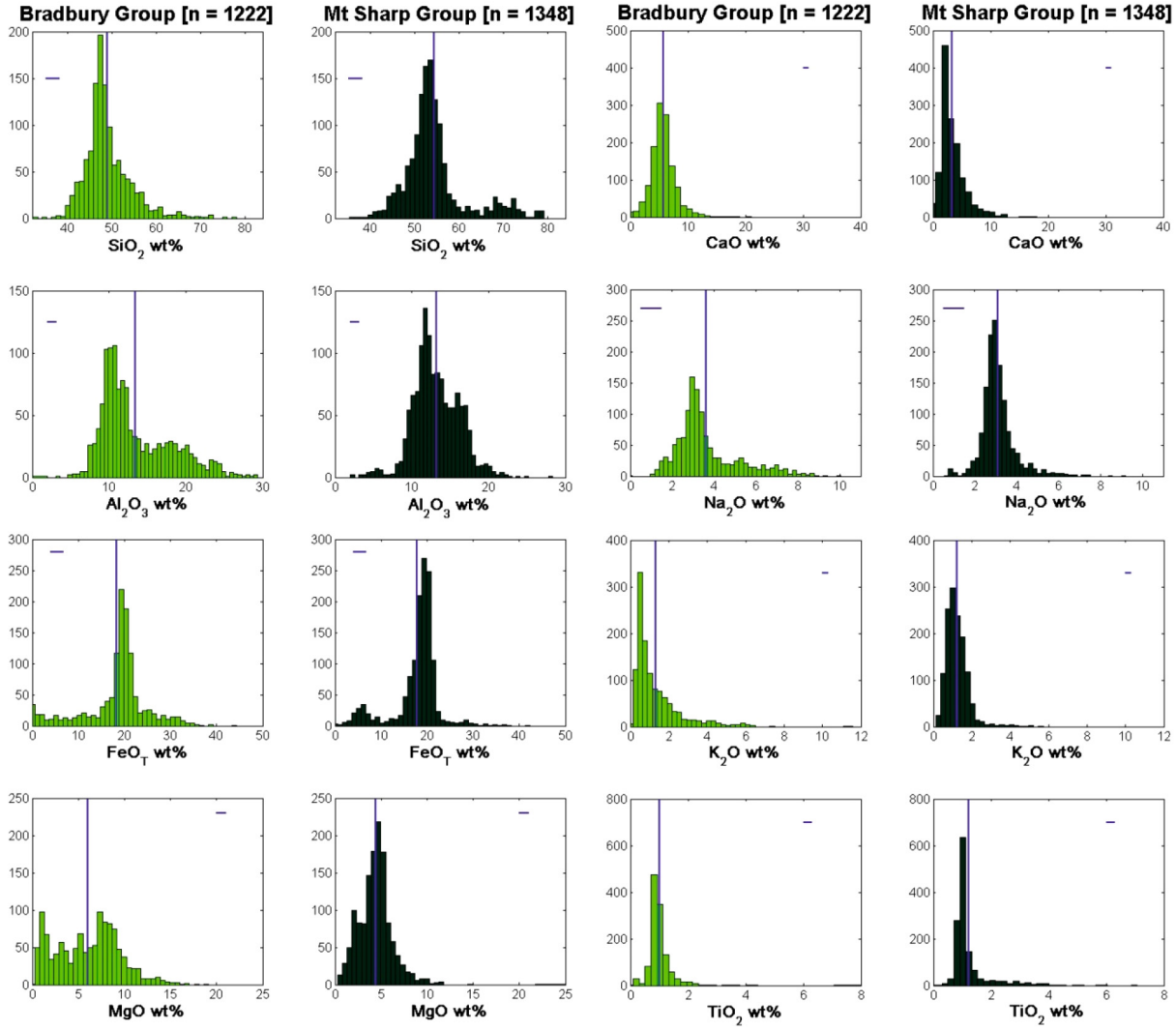

Fig. 5. Major element histograms for the Bradbury (light green, n = 1222) and Mt Sharp (dark green, n = 1371) stratigraphic groups presenting the data distribution for the constrained bulk rock ChemCam dataset of sedimentary outcrop. The blue vertical lines represent the mean composition, and the horizontal lines show the standard deviation (1σ). (For interpretation of the references to colour in this figure legend, the reader is referred to the web version of this article.)

correspond to the pronounced tails in the histograms or, in the cases of Al_2O_3 and MgO, to the secondary histogram peaks (Fig. 5).

The Mt. Sharp Group (Murray formation, sols 755–1482) has contours centred on a single focus for FeO_T, K_2O, Na_2O, and TiO_2 when plotted against SiO_2 (Fig. 6), though slight bimodality is shown in the FeO_T histogram with a small peak at 5.6–6.6 wt%, and a large peak at 18.9–19.9 wt%. SiO_2 and Al_2O_3 density contours and histograms show slight bimodality (peaks at 53.1–54.1 and 67.7–68.7 wt% SiO_2, 11.5–12.0 and 15.7–16.2 wt% Al_2O_3), as does MgO versus SiO_2 to a lesser extent. The low MgO subpopulation at high SiO_2 in the Harker plot contours deviate from the respective modal compositions (Fig. 6.D) and correlate with the minor SiO_2 peak of ~70 wt% shown in Fig. 5A.

Calcium oxide contents are notably lower in the Mt Sharp Group with mean, peak and focal compositions all <3.4 wt% (Figs. 5 & 6 and Table 1). Mt Sharp Group total FeO and Na_2O focal compositions are similar to those of the Bradbury Group (Figs. 5, 6), but with less variability between these oxides and SiO_2, indicated by the contours centred more uniformly on the foci. The Mt. Sharp Group has a higher mean SiO_2 content (54.4 wt% vs. 49.0 wt% for the Bradbury Group, Table 1), which is reflected in its density contours with average focal compositions centred around 53.1 ± 1.9 wt% SiO_2 (Fig. 6 and Table 3). Though not identified in mean compositions, the density contour plots also show that Mt Sharp Group focal compositions are more elevated in Al_2O_3 (12.1 ± 0.8 wt%) and K_2O (1.2 ± 0.2 wt%) than Bradbury (foci at 10.6 ± 1.2 wt% and 0.5 ± 0.3 wt% respectively). Overall, the Mt Sharp

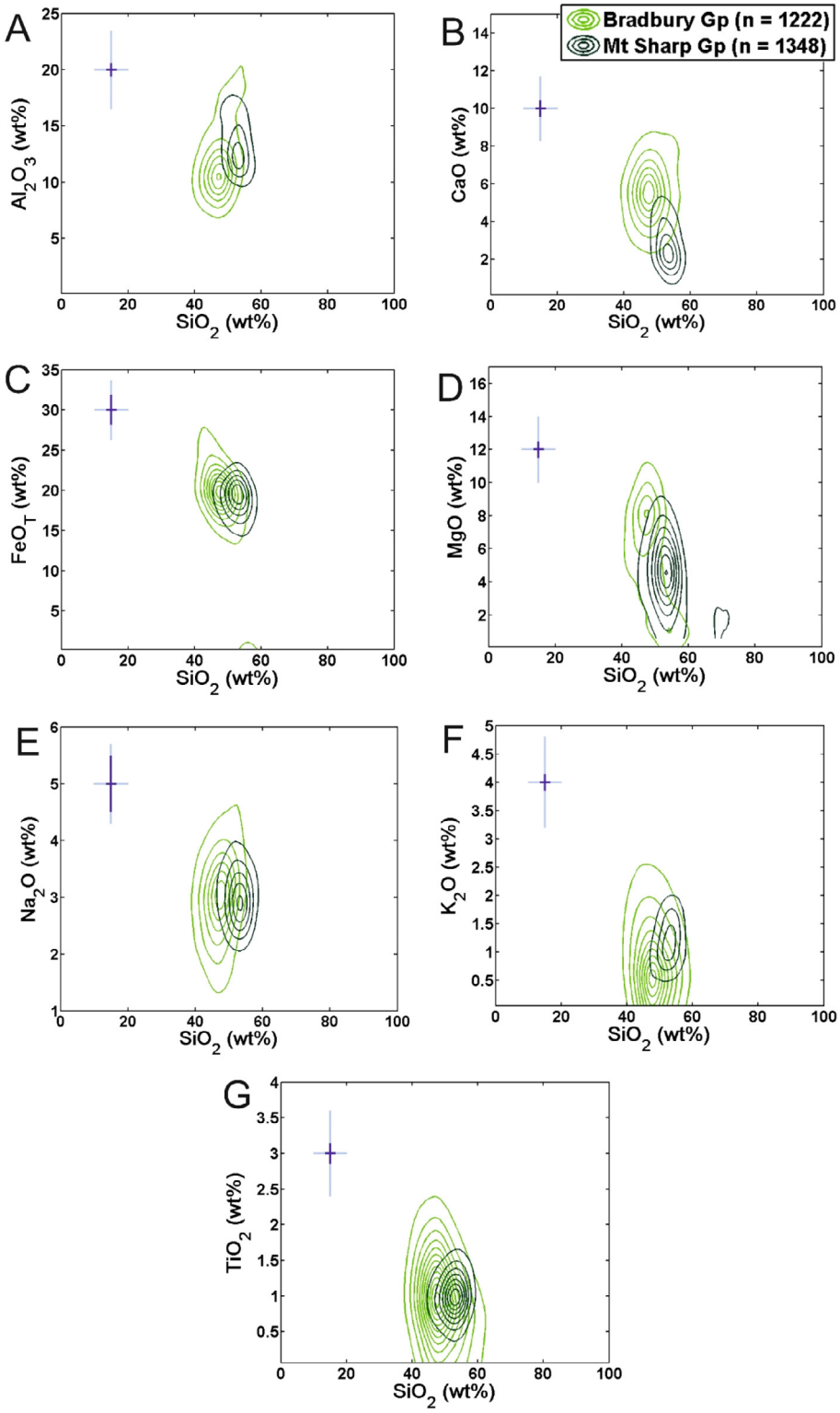

Fig. 6. Harker density contour plots of the constrained ChemCam bulk rock dataset plotted according to related stratigraphic groups; Bradbury (light green) and Mt Sharp (dark green), with SiO_2 on the x-axis and major element oxide on the y-axis. The light blue cross represents ChemCam accuracy (RMSEP), the dark blue cross shows precision (1σ). (For interpretation of the references to colour in this figure legend, the reader is referred to the web version of this article.)

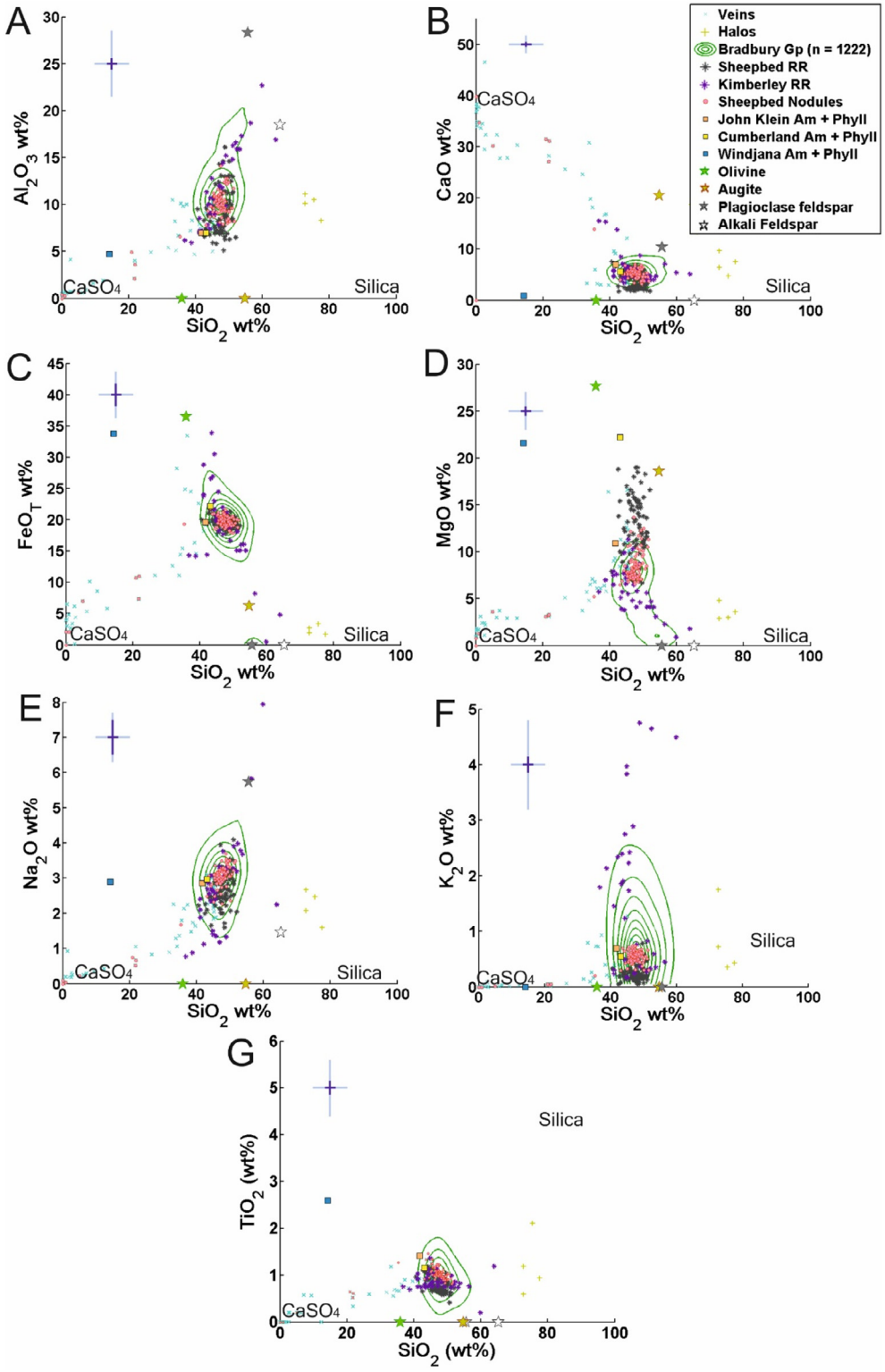

Fig. 7. Harker density contour plots of Bradbury Group constrained bulk composition (light green density contours) and alteration trends, with SiO_2 on the x-axis and major element oxide on the y-axis. Each scatter point for the alteration features represents a ChemCam observation point composition for mineral vein, fracture-associated halo, nodule and raised ridge targets. The light blue cross shows ChemCam accuracy (RMSEP), the dark blue cross shows precision (standard deviation). Calculated CheMin amorphous and phyllosilicate compositions (Vaniman et al., 2014; Treiman et al., 2016) are plotted as squares with Gale primary igneous minerals refined from the CheMin unit-cell parameters (olivine, augite, plagioclase and sanidine) shown as stars. RR = Raised ridges, Am + Phyll = amorphous + phyllosilicate component, $CaSO_4$ = calcium-sulfate which may be in various hydration states, Silica = silica-enrichment. (For interpretation of the references to colour in this figure legend, the reader is referred to the web version of this article.)

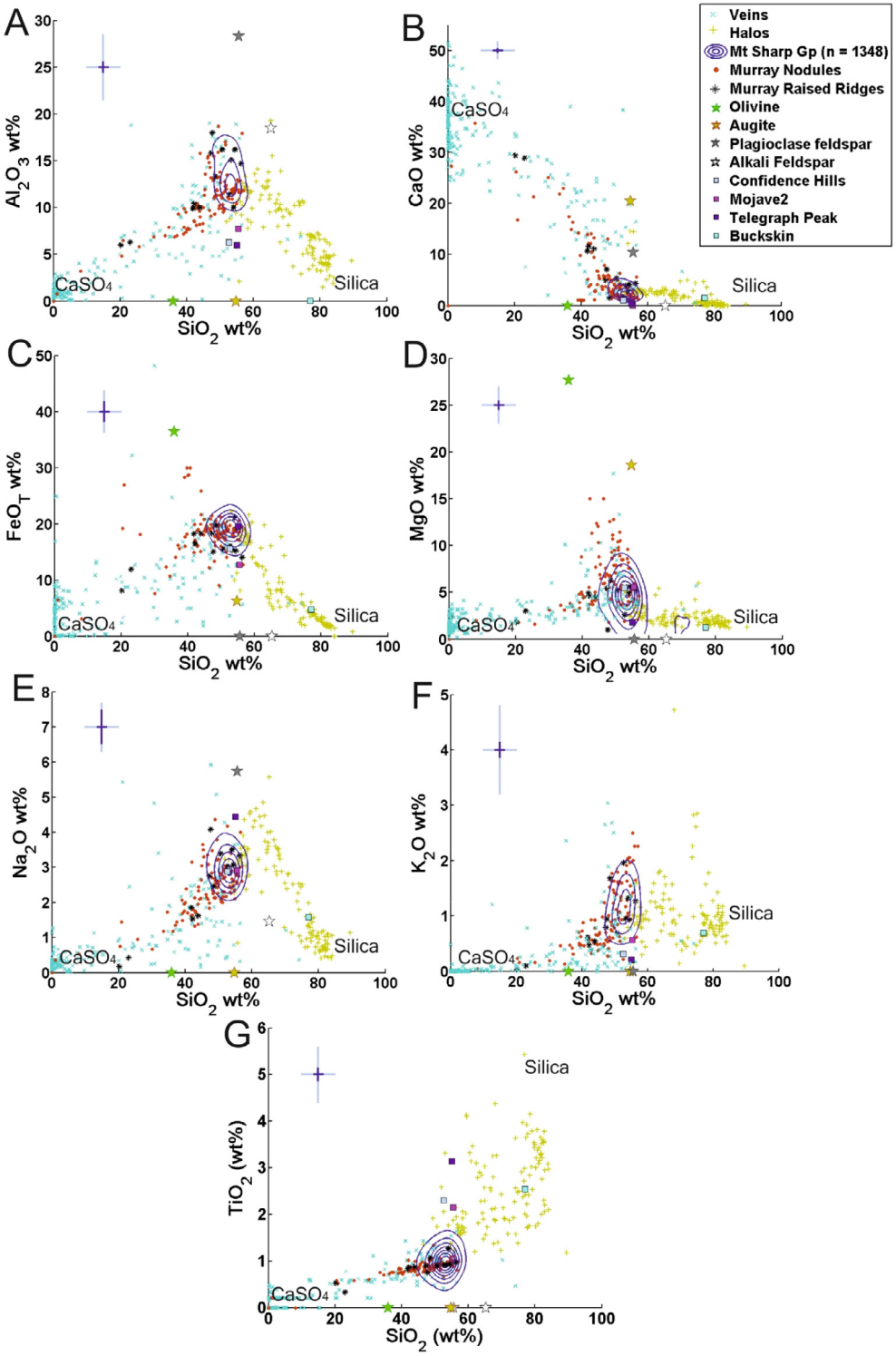

Fig. 8. Harker density contour plots of Mt Sharp Group constrained bulk composition (dark green density contours) and alteration trends, with SiO_2 on the x-axis and major element oxide on the y-axis. Each scatter point for the alteration features represents a ChemCam observation point composition for mineral vein, fracture-associated halo, nodule and raised ridge targets. The light blue cross shows ChemCam accuracy (RMSEP), the dark blue cross shows precision (standard deviation). Calculated CheMin amorphous and phyllosilicate compositions (Rampe et al., 2017a) are plotted as squares, Gale primary igneous minerals refined from the CheMin unit-cell parameters (olivine, augite, plagioclase and sanidine) are shown as stars. RR = Raised ridges, Am + Phyll = amorphous + phyllosilicate component, $CaSO_4$ = calcium-sulfate which may be in various hydration states, Silica = silica-enrichment. (For interpretation of the references to colour in this figure legend, the reader is referred to the web version of this article.)

Table 1
Basic ChemCam statistics showing the mean, standard deviation (StDev), Minimum, Median, Maximum and Range across each major element oxide for the Bradbury and Mt Sharp stratigraphic groups.

Variable (wt%)	Unit	Mean	StDev	Minimum	Median	Maximum	Range
SiO_2	Bradbury	49.0	5.2	34.4	48.0	77.6	43.2
	Mt Sharp	54.4	7.0	36.0	53.2	78.8	42.8
TiO_2	Bradbury	1.0	0.6	0.0	0.9	13.1	13.1
	Mt Sharp	1.2	0.7	0.0	1.0	7.0	7.0
Al_2O_3	Bradbury	13.5	4.6	3.3	11.9	29.1	25.8
	Mt Sharp	13.2	3.0	2.4	12.8	27.9	25.5
FeO_T	Bradbury	18.3	7.0	0.0	19.6	43.7	43.7
	Mt Sharp	17.8	5.2	0.1	19.0	41.7	41.6
MgO	Bradbury	6.0	3.5	0.3	6.4	19.0	18.7
	Mt Sharp	4.4	1.8	0.4	4.4	14.8	14.4
CaO	Bradbury	5.7	2.2	0.0	5.6	20.8	20.8
	Mt Sharp	3.4	2.2	0.2	2.7	17.1	16.9
Na_2O	Bradbury	3.6	1.5	1.0	3.2	9.9	8.9
	Mt Sharp	3.1	0.8	0.7	3.0	9.2	8.4
K_2O	Bradbury	1.3	1.2	0.1	0.8	11.4	11.3
	Mt Sharp	1.2	0.6	0.2	1.1	5.5	5.4

Group has a smaller, more uniform, range in major element compositions than the Bradbury Group (Table 1 and Table 3).

3.1.1. Constrained bulk rock Simple Linear Regression (SLR) models and correlation coefficients

We use SLR models and Pearson correlation coefficients to calculate element correlations for the constrained stratigraphic group and unit datasets in order to show which minerals dominate sediment geochemistry and whether or not alteration has affected these sediments on a scale not identifiable by the MSL imaging instruments. SLR models of the constrained bulk rock dataset for the Bradbury and Mt Sharp stratigraphic groups both show strong negative correlations between FeO_T and SiO_2 (r values of −0.85 and −0.49 respectively; see Figs. 6C & 7C). In these models, the null hypothesis tests for no correlation between the variables in question (H_0: $\rho = 0$). Therefore, the strong negative correlations between FeO_T and SiO_2 are statistically significant as their p-values are much lower than the significance level at $\alpha = 0.05$ (Fig. B.1, and Tables B.1 and B.2. of Appendix B). Strong positive correlations ($r > 0.5$) also exist in both groups for Al_2O_3 and Na_2O, with the Bradbury Group demonstrating the best fit ($r = 0.86$), and the Mt Sharp Group substantially lower ($r = 0.60$) due to scatter towards elevated Na_2O concentrations (see Fig. 7 and Appendix Fig. B.2).

Both the Bradbury and Mt Sharp Groups have positive correlations between MgO versus FeO_T, and negative correlations between MgO against Al_2O_3 and MgO versus Na_2O. When plotted, MgO displays a curvilinear trend for MgO against Al_2O_3 (Fig. B.3 in the Appendix). This curvilinear trend is fitted best to Bradbury Group data ($r^2 = 75.5\%$), and worst to the Mt Sharp Group ($r^2 = 0.6\%$), indicative of no fit in the latter case. The Mt Sharp Group SLR models with the weakest fit to the curvilinear regression lie towards the origin of Al_2O_3 and MgO. These data points with residuals that do not fit the regression line are targets in the Marias Pass, silica-rich area.

3.1.2. Constrained bulk rock Al_2O_3 Multiple Linear Regression (MLR) model results

Results from the stratigraphic group Al_2O_3 MLR models (Section 2.2) show that all predictors (SiO_2, TiO_2, FeO_T, MgO, CaO, Na_2O, and K_2O) significantly contribute to the Bradbury Group MLR model (p-value $< \alpha$), and all predictors except K_2O (p-value = 0.60) contribute significantly to the Mt Sharp Group MLR model. This suggests a weak association of K_2O with the other predictors in the Mt Sharp Group model. Removal of K_2O from the model does not significantly improve the fit, so we do not exclude K_2O as a predictor. Both models have high adjusted r^2 values with Bradbury $r^2 = 87.1\%$ and Mt Sharp $r^2 = 67.3\%$ which shows the goodness-of-fit of the MLR models to the dataset.

For the Bradbury Group, the modelled percentage contributions of Na_2O (74.5%), K_2O (4.7%), and MgO (4.6%) demonstrate that they contribute the most to Al_2O_3 variation while FeO_T (0.3%) and TiO_2 (0.04%) contribute the least in this regression model. All predictors have negative coefficients in relation to the response with the exception of Na_2O and K_2O that are positive. In the Mt Sharp Group, SiO_2 (22.2%), FeO_T (20.9%), and Na_2O (9.9%) contribute the most to the model, with K_2O (0.01%) and CaO (3.7%) providing the smallest contributions. For the Mt Sharp Group, predictor coefficients show that as Al_2O_3 increases, all major elements except Na_2O decrease.

Table 2
Average Chemical Indices of Alteration (CIA; Nesbitt and Young, 1982) values for ChemCam observation point analyses taken at the stratigraphic group and unit scale for the constrained host rock dataset. The equation for CIA is calculated using molar abundances and shown below.

Group CIA (%)	Bradbury	Mt Sharp	$CIA = \frac{Al_2O_3}{(Al_2O_3 + CaO + Na_2O + K_2O)}$						
ChemCam Strat. Unit CIA (%)	43 ± 9 Sheepbed	52 ± 8 Gillespie Lake	Glenelg	Darwin	Kimberley	Murray-Pahrump Hills	Murray-E Nauk.	Murray-W Nauk.	Murray-Buttes
ChemCam	40 ± 4	45 ± 9	42 ± 8	44 ± 8	39 ± 8	51 ± 6	53 ± 8	54 ± 6	55 ± 5
APXS*	34 ± 2					45 ± 4			

* APXS values reported by Hurowitz et al. (2017).

3.2. Alteration feature major element variation and correlations

Figs. 7 and 8 highlight the major element trends associated with alteration features identified within each stratigraphic group, and isolated from the constrained bulk rock dataset (see Section 2.3). The stratigraphic group density contours, CheMin derived amorphous and phyllosilicate (AP) components, and common primary, detrital, silicate minerals (olivine, plagioclase, alkali feldspar, and augite) are also plotted to help distinguish alteration trends from detrital igneous mineral mixing trends. Alteration features were identified within each stratigraphic group, and are presented as scatter points over the bulk rock density contours.

3.2.1. Sulfate mineral veins and fracture-associated alteration halos

Sulfate mineral veins (Fig. 4C) exhibit high calcium enrichment (Figs. 7 and 8), low abundances of other oxides, and low totals. Meanwhile, diagenetic halos (Fig. 4D), ~50 cm in width (Yen et al., 2017), are associated with an increase in silica content of the host rock (Frydenvang et al., 2017; Yen et al., 2017) and share similar elemental compositions to the high silica targets analysed at the Buckskin drill hole on sol 1057 (Fig. 8; Morris et al., 2016). The halos mostly occurred in the Mount Sharp Group, particularly between Marias Pass and Bridger Basin (Frydenvang et al., 2017; Yen et al., 2017). However, one possible halo was observed in the Bradbury Group, with the target Kukri at Darwin, on Sol 392 (Williams et al., 2014).

Within fracture-associated alteration halos FeO_T and Na_2O possess the best-defined negative correlations against SiO_2, giving strong Pearson's correlation coefficients of −0.90 and −0.82 respectively. The only element to show a (weak) positive correlation with halo SiO_2 enrichment is TiO_2 ($r = 0.29$, t-test p-value $< \alpha$). Al_2O_3 and Na_2O show the strongest positive correlation ($r = 0.92$), and display the best-defined negative trends when plotted against SiO_2, along with FeO_T (Figs. 8, 9). MgO concentrations appear to be relatively uniform at ~3.0 wt%, except at $SiO_2 > 80$ wt% where concentrations remain at ~1.0 wt%.

Stratigraphic group density contours in our constrained bulk dataset do not appear to have been influenced by either the calcium-sulfate mineral veins or the silica-rich halos (Figs. 7, 8). However, despite measures taken to remove the effects of diagenetic silica enrichment in the Marias Pass area, scatter plots of the Marias Pass observation point compositions follow a silica-rich alteration trend (e.g., Fig. C.1. in Appendix C). The Marias Pass observation points were not removed from the bulk dataset as they constitute a small proportion of data points and hence, have not affected the overall stratigraphic group density contour focal compositions.

3.2.2. Raised ridges

Erosion resistant raised ridge features (Fig. 4A) occur across both stratigraphic groups (Figs. 7 and 8). Bradbury raised ridges (BRR), are present in both the Sheepbed Member and Kimberley formation and show

variable Al_2O_3 5.1–22.7 wt% relative to the Bradbury density contour focus at 10.6 ± 1.2 wt%. MgO concentrations can extend up to 20 wt%, with BRR features demonstrating a slight depletion in Na_2O, and some scatter towards elevated K_2O concentrations. When the BRR are subdivided (Fig. 7) into Sheepbed raised ridges and the two raised ridges analysed by ChemCam at the Kimberley waypoint (targets Roebuck on sol 584 and Loadstone on sol 625), it is evident that the Sheepbed BRR are more enriched in MgO, and depleted in CaO and K_2O compared to the Bradbury host rock (Fig. 7). The results for the Sheepbed raised ridges are consistent with the results of Leveille et al. (2014) who reported similar element enrichments and depletions for raised ridges at this locality. On the other hand, the Kimberley BRR are generally more enriched in K_2O, and depleted in MgO, with substantial scatter for Al_2O_3, CaO, Na_2O, and FeO_T relative to bulk rock (Fig. 7). Fewer raised ridges were identified within the Mt Sharp Group (MRR) compared to the Bradbury Group. MRR are usually located at vein or fracture margins, and either possess a similar geochemical composition to the bulk Mt Sharp Group composition, or they follow the same CaO enrichment trend as the calcium-sulfate mineral veins (Fig. 8).

3.2.3. Nodules

Bradbury Group nodules (Fig. 4B) were predominately identified in the Sheepbed Member mudstone within "nodule-rich" bedrock (Stack et al., 2014b). Sheepbed nodules are spheroidal, at the mm-scale, and can be divided into three groups (solid, hollow, or filled) depending on their internal structure (Stack et al., 2014b). Solid nodules do not show obvious internal structures, are similar in texture and colour to the host rock and contribute the majority of ChemCam nodule analyses. Hollow nodules possess raised rims and internal depressions. Finally, filled nodules classify those that contain light-toned, sulfate minerals (Stack et al., 2014b). ChemCam targets from the Sheepbed nodule-rich bedrock show minimal deviation from bulk rock composition (Fig. 7). Similar to Bradbury Group nodules, the nodule features identified in the Mt Sharp Group are also mm-scale and of a similar colour to the surrounding bedrock, though these are less frequent and have more irregular shapes (Nachon et al., 2017). Unlike the Sheepbed nodules, Mt Sharp Group nodules do not show any obvious internal structure. Nodules of the Mt Sharp Group have similar geochemical trends to the calcium-sulfate mineral veins (major element depletion in SiO_2 and the alkalis, plus most points showing Al_2O_3 and FeO_T depletion with CaO enrichment).

4. DISCUSSION

4.1. Chemical alteration of Gale crater sediments

Chemical weathering on Mars has been relatively low compared to Earth for most of the planet's history as evidenced by the high abundance of ancient unweathered basaltic material on the Martian surface (Hoefen et al., 2003; Hausrath et al., 2008; McSween et al., 2009), and the paucity of chemical weathering products in Amazonian-aged terrains (e.g., Ehlmann et al., 2013). Instead, mechanical and physical weathering processes have dominated sediment generation (Bandfield et al., 2000; Christensen et al., 2001; McLennan et al., 2014). The majority of our constrained bulk rock major element correlations point towards the importance of detrital primary minerals in Gale's sedimentary record. The dominant negative correlation trend for both stratigraphic groups in our constrained bulk rock dataset is FeO_T against SiO_2. The Bradbury Group also has notably strong negative correlations between MgO against Al_2O_3, and MgO against Na_2O. The only significant positive correlation trend is Na_2O versus Al_2O_3. These correlations extend throughout the stratigraphic succession. They are expressed through the elongation of density contours in the direction of CheMin-derived olivine, augite, and feldspar compositions (Figs. 7 and 8) and are therefore likely related to mafic versus felsic mineral abundances. The strong positive association of Al_2O_3 in the MLR models with Na_2O (and K_2O for the Bradbury Group), and negative association with FeO_T and MgO are also indicative that felsic/mafic mineral proportions are the controlling factors on bulk stratigraphic unit geochemistry.

The minerals that appear to dominate compositional variation within Gale's sedimentary units constitute on average ~40–70% in all CheMin analyses and are of primary igneous origin (for CheMin mineral compositions, see Appendix A). The other ~30–60% in CheMin analyses relate to the amorphous and phyllosilicate component (Fig. 9 and discussed in Section 4.1.2; for compositions see Appendix A). Secondary minerals suggest that chemical weathering is recorded to some extent in the ChemCam target analyses included in our constrained bulk rock dataset. The abundance of alteration features in Gale crater's stratigraphy is also evidence of aqueous alteration, likely the result of diagenetic episodes. Distinguishing alteration trends relating to these diagenetic episodes and chemical weathering from source rock characteristics is essential before any conclusions on source region chemistry can be made.

4.1.1. Element mobility and feature-related weathering

We have used major element trends of observed diagenetic features to determine the extent of alteration that has occurred in our constrained bulk rock dataset (Figs. 7, 8). As described in Section 3.2.2, the late-stage diagenetic features (mineral veins and silica-rich halos) which cross-cut stratigraphic units show clear compositional trends away from all stratigraphic group compositions (Figs. 7, 8).

For the silica-rich halos, ChemCam analyses plot away from constrained contour compositions suggesting that element mobilisation was restricted to the associated fracture zones (Frydenvang et al., 2017; Yen et al., 2017). The one exception is the Marias Pass area of the Murray formation presented in Section 3.2.2 whose compositions follow a similar trend to the silica-rich halos. This could be related to the SiO_2 polymorph grains that are abundant in the

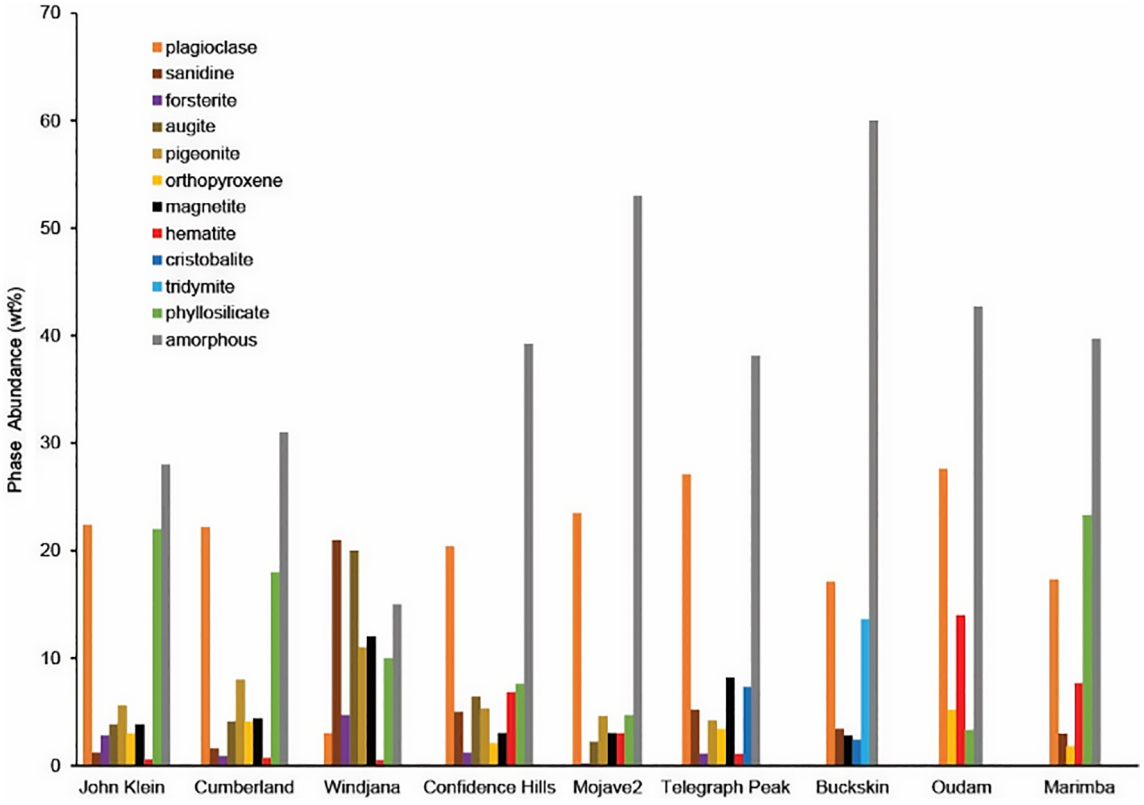

Fig. 9. Crystalline abundance of minerals in weight % (Vaniman et al., 2014; Treiman et al., 2016; Rampe et al., 2017a; Morris et al., 2016; Morrison et al., 2018) and amorphous abundance (Rampe et al., 2017a; Morrison et al., 2018) [y-axis] for each drill hole taken in the Bradbury (John Klein, Cumberland, and Windjana) and Mt Sharp (Confidence Hills, Mojave2, Telegraph Peak, Buckskin, Oudam, and Marimba) stratigraphic groups.

Buckskin drill hole (Morris et al., 2016), and which would plot at a similar position on the Harker diagrams to the fracture-associated halo alteration trends (Fig. 8). Alternatively, the Marias Pass Lion outcrop (sols 1053–1066) where the Buckskin drill hole was conducted and ChemCam observation points acquired, does possess the near white, light-toned, visual characteristic of the alteration halos. These outcrops are also located near light-toned, fracture-associated halos in the overlying Stimson formation (Frydenvang et al., 2017). Therefore, it is difficult to distinguish whether the Marias Pass target igneous mineralogy and source composition have been overprinted by secondary alteration processes of the fracture-associated halo alteration. As Marias Pass analyses represent a small set of outlying Mt Sharp Group compositions that plot far from the main Mt Sharp Group contours (Fig. 8), this silica-rich endmember and halo diagenesis has not influenced the density contour compositions for the constrained bulk Murray dataset. Hence, we have not recalculated the Murray formation contours, but have excluded Marias Pass data in the Chemical Index of Alteration analysis of Section 4.1.3.

Scatter trends associated with the light-toned mineral vein features demonstrate a clear trend away from host rock compositions towards CaO enrichment (Figs. 7, 8) which supports the interpretation that these are predominately calcium-sulfate mineral veins (Nachon et al., 2014; Rapin et al., 2016; L'Haridon et al., 2018). They are thought to be dominated by bassanite in ChemCam surface analyses (Rapin et al., 2016) but some appear more hydrated below the surface as exposed by the drill (L'Haridon et al., 2018; Vaniman et al., 2018). The total sum of oxides also becomes lower as a result of not directly analysing sulfur in the Ca-sulfate veins (Rapin et al., 2016). Overall, the Bradbury Group and Mt Sharp Group density contours do not appear to have been influenced by this set of alteration features (Figs. 7, 8) indicating that the compositional influence relating to these diagenetic features was successfully removed from the constrained bulk rock dataset.

Many nodule compositions reflect bulk rock composition, particularly those of the Bradbury Group (Fig. 7, Stack et al., 2014b), which could either indicate that these observation point analyses have proportionally sampled more host rock, or that these features have formed by closed system alteration preserving geochemical source characteristics. The nodules that show geochemical variation away from bulk composition, such as those at the base of the Mt Sharp Group, appear to relate to sulfate precipitation (Fig. 8 and Nachon et al., 2017). They follow similar major element trends as the mineral veins, but this time with magnesium- as well as calcium-sulfates dominating

the geochemical composition (Figs. 7 and 8; Nachon et al., 2017). In the Mt Sharp Group, a few nodule analyses show high FeO_T compositions >25.0 wt% (Fig. 8C). We interpret these FeO_T-rich nodule analyses as potentially showing iron-oxides, as they are low in concentration for the other major elements with respect to bulk Mt Sharp. This is in contrast to the high-FeO_T composition of the ChemCam target Hayden Peak (sol 785) that Nachon et al. (2017) interprets to be Na-jarosite due to its high Na_2O compared to other Pahrump diagenetic features. As the nodules of the Bradbury Group do not deviate significantly from the Bradbury density contours, it is likely that they resulted from closed system alteration at the scale of the stratigraphic units. However, the association of sulfates with nodules in the Mt Sharp Group indicates more open system conditions, similar to the sulfate veins, to contribute the excess CaO and MgO. With these nodules removed from the constrained bulk rock dataset, the geochemical effect of open system alteration on the Mt Sharp Group constrained dataset is minimised.

The geochemical compositions of raised ridges in Gale crater vary according to stratigraphic unit (Figs. 7 and 8). Bradbury Group raised ridges show enrichments in either MgO or K_2O, Na_2O, and Al_2O_3, while raised ridges identified in the Mt Sharp Group appear to be geochemically related to calcium-sulfates comparable to the Mt Sharp Group nodules (Fig. 8). Aqueous alteration models of raised ridges in the Bradbury Group Sheepbed mudstone show that their high MgO concentrations likely occurred as a result of olivine dissolution in a closed system with a low water-rock ratio (Leveille et al., 2014; McLennan et al., 2014; Bridges et al., 2015). The enrichment in K_2O, Na_2O, and Al_2O_3 for the Kimberley formation raised ridges could relate to a similar process but with feldspar dissolution, particularly due to the high total mass abundance (26.8%) of felsic minerals in the Windjana drilled sample (Treiman et al., 2016; Morrison et al., 2018). As the raised ridge features have been removed from the constrained database, the local, post-depositional remobilisation of these elements is minimised.

4.1.2. Gale crater amorphous and phyllosilicate components

Due to the lithified nature of the ChemCam host rock targets, some diagenesis will have occurred on a scale smaller than that of MAHLI image resolution (13.9 μm at a standoff distance of 2 cm; Edgett et al., 2012) during the cementation of the mud and sandstone units. For this reason, we compare the geochemical compositions modelled from CheMin and APXS analyses for the amorphous and phyllosilicate (AP) components (Vaniman et al., 2014; Treiman et al., 2016; Rampe et al., 2017a) to our constrained bulk rock dataset. In Figs. 7 and 8, we represent the composition of the X-ray amorphous and phyllosilicate components as a single point for each sample, based on the bulk composition and the calculated composition of the crystalline phases identified by CheMin (e.g., Morrison et al., 2018). In actuality, there is a range of potential AP compositions because of the uncertainties in mineral and amorphous abundances and refined crystal chemistry of major minerals calculated from CheMin data (e.g., Dehouck et al., 2014). We plot the best estimate of the AP compositions, rather than the range of potential compositions, to simplify the diagrams.

All of the Bradbury and Mt Sharp Group's 9 drilled samples in the region included here possess varying abundances of an amorphous component, up to 60 % in the Buckskin drill hole (Morris et al., 2016). The origin of this amorphous component in Gale crater has been hypothesised to either relate to detrital, and then subsequently altered soil or aeolian material (Dehouck et al., 2014; Vaniman et al., 2014), diagenetic cement (Treiman et al., 2016), or chemically altered and weathered volcanic glass (Bish et al., 2013; Rampe et al., 2017a). Excluding the Marias Pass area, the Mt Sharp Group has ~10–15% greater amorphous component than the Bradbury Group Sheepbed mudstones, which additionally possess a ~10% greater abundance of phyllosilicates than the Mt Sharp mudstones reported here (Murray formation; Fig. 9).

Most AP components in mudstone units (John Klein, Mojave 2, Telegraph Peak, Confidence Hills, Marimba, with the exception of Cumberland and Buckskin) are within ChemCam instrument error of their associated stratigraphic group constrained bulk rock geochemistry (Figs. 7, 8), with some slight variations relative to their Group focus. For the purposes of our study we note that AP in the mudstone units does not demonstrate consistent enrichments in Al_2O_3 or SiO_2, or a consistent loss of divalent and monovalent cations relative to either the constrained ChemCam calculated bulk compositions presented here or in the APXS bulk compositions (Rampe et al., 2017a). Hence, Gale crater mudstone AP component may largely reflect local variations in mineralogy of the stratigraphic units that have undergone relatively closed system diagenesis as calculated AP compositions do not show the expected trends for open system aqueous alteration.

MgO-enrichment in the Cumberland AP component of the Sheepbed mudstone relative to the Bradbury bulk rock composition has been attributed to olivine saponitisation (Dehouck et al., 2014; Vaniman et al., 2014). The mean phyllosilicate abundance in the Sheepbed Member is ~20% (Vaniman et al., 2014). Different 001 spacing within CheMin for the John Klein and Cumberland smectites suggests that the elevated MgO component in Cumberland most likely relates to a $Mg(OH)_2$-rich interlayer site in the smectite component that is absent in the collapsed smectite analysed at John Klein (Vaniman et al., 2014; Bristow et al., 2015). In addition, MgO enrichment in the Cumberland AP component follows the trends of enrichment similar to the Sheepbed raised ridges and nodules (Fig. 7; Leveille et al., 2014), supporting the conclusions of Vaniman et al. (2014) and Bristow et al. (2015) that the Cumberland drill hole has sampled one of these diagenetic features. Therefore, the greater abundance of Mg^{2+} in the Cumberland phyllosilicates is likely a consequence of the aqueous alteration that formed these diagenetic features. This MgO-rich AP component will have consequently been removed from the constrained bulk rock dataset with the exclusion of raised ridge features.

The other mudstone sample whose AP component demonstrated a distinct composition relative to the bulk

Mt Sharp Group focal composition is the Marias Pass Buckskin drilled sample. The Buckskin sample contains no phyllosilicate (Morris et al., 2016; Rampe et al., 2017a) and possesses strong enrichment in SiO_2 and TiO_2, as well as a depletion in FeO_T, relative to the Mt Sharp Group density contours. These major element trends are similar to those of its host rock whose composition may either relate to the silica-rich volcanic source region that formed the tridymite (Morris et al., 2016), or the fracture-associated alteration halos. Hence, this mudstone amorphous component may have also been derived from a similar process (Section 4.1.1).

The Windjana drill hole AP composition of the Kimberley formation is distinct from the mudstone and bulk Bradbury geochemistry, likely as a result of its sandstone grain size (Treiman et al., 2016) resulting in greater porosity and enabling a higher permeability and pore water content. Windjana AP possesses strong enrichments in FeO_T and MgO with depletions in SiO_2, CaO, and K_2O relative to the bulk Bradbury Group compositions (Fig. 7). The higher pore water content of the Windjana sandstone relative to the mudstone units may have inhibited pressure solution upon compaction, more so than in the finer grained units. This would have restricted extensive element remobilisation within the unit similar to cementation of terrestrial sandstones (McKinley et al., 2011; Henares et al., 2014), making the compositions of the AP component more distinct compared to that of the bulk rock. High concentrations of FeO_T have been observed in all of Gale crater's sedimentary units analysed so far by MSL (Grotzinger et al., 2014, 2015). The iron content of sedimentary units in Gale crater has been suggested to be associated with iron-rich cement (Blaney et al., 2014; Grotzinger et al., 2014; Vaniman et al., 2014; Anderson et al., 2015) that may have formed through isochemical alteration with an iron-rich fluid (Grotzinger et al., 2014; Bridges et al., 2015; Hausrath et al., 2018). This likely led to the precipitation of magnetite in the Windjana sandstone and an iron-rich AP component hypothesised to relate to ferrihydrite and/or an Fe/Mg smectite (Treiman et al., 2016). These hypothesised iron-rich phases for the Windjana AP component are based on CheMin XRD amorphous diffraction intensities and the SAM evolved gas analysis broad water release of the Windjana drilled sample (Treiman et al., 2016).

The presence of alteration phases derived from early stages of alteration e.g., smectites and Fe-oxides (Treiman et al., 2016; Rampe et al., 2017a; Rampe et al., 2017b), and lack of secondary mineral phases such as Al-clays indicative of environments subject to extensive leaching (Rampe et al., 2017a, 2017b) suggests minimal open system weathering. This, together with the compositions of mudstone AP that do not substantially deviate from the ChemCam constrained bulk rock compositions (except the sandstone Windjana, and potentially altered Cumberland and Buckskin drill holes) suggests isochemical weathering in a closed system for samples in our constrained bulk rock dataset (Fig. 8). With obvious diagenetic features e.g., halos, ridges, nodules, veins removed from the constrained ChemCam bulk rock dataset (Sections 2.3 and 3.2), and by only considering point analyses with total sum of oxides between 95–105 wt%, chemical trends across stratigraphic units should be generally representative of detrital source compositions and/or mineral sorting processes.

4.1.3. Chemical index of alteration

As we have distinguished and isolated the compositional effects of diagenesis in the previous sections, we now proceed to use the Chemical Index of Alteration (CIA) to determine the extent of chemical weathering in the sediments' source regions. CIA (Nesbitt and Young, 1982) is a method to quantitatively determine how chemically weathered a sample is according to the susceptibility of silicate minerals to chemical remobilisation, e.g., feldspar to clay alteration. CIA values ($Al_2O_3/(Al_2O_3 + CaO + Na_2O + K_2O)$) have been used to gauge the extent of open system chemical weathering at the source or during sediment transportation for Gale crater (e.g., McLennan et al., 2014; McLennan et al., 2015; Le Deit et al., 2016; Schieber et al., 2017; Siebach et al., 2017; Hurowitz et al., 2017; Mangold et al., 2017a; Mangold et al., 2018). On Earth, where carbonates represent a significant fraction of the sedimentary budget, CIA values are corrected to only account for silicate-bound Ca (Nesbitt and Wilson, 1992). Carbonates are more localised on Mars in comparison to Earth (Ehlmann et al., 2008; Bridges et al., 2019), and only traces of carbonates have been found in Gale crater (Archer et al., 2014). Ca-sulfates may, however, have been introduced to the sediment from external sources during burial and diagenesis (Schieber et al., 2017). To correct for this, targets containing sulfates have been removed from the bedrock dataset, as described in Sections 2.3 and 3.2.1., although indigenous sulfate minerals in the bedrock appear to be rare for the part of the rover traverse considered in this study (sols 1–1482). Some minor phosphates abundances have been described (Forni et al., 2015; Rampe et al., 2017a; Meslin et al., 2018). Because of the possibility of some non-Si-bound Ca in these calculations, the CIA values determined here should be considered as a minimum (Mangold et al., 2017a). CIA values for the stratigraphic groups and units (along with equations) are given in Table 2 based on both APXS and ChemCam data. Despite Marias Pass targets being included in the constrained bulk rock dataset for the Mt Sharp Group, they are not included in the CIA calculations due to their apparent very different mineralogy (e.g., tridymite; Morris et al., 2016) and/or post-depositional aqueous alteration related to the silica-rich fracture-associated halos (see above, Section 4.1.1). CIA values have also been calculated for ChemCam data by Mangold et al. (2018) for various portions of the Murray formation of the Mt. Sharp group.

Constrained ChemCam bulk rock analyses in the Bradbury Group demonstrate a low average CIA (43 ± 9, Table 2) indicative of minimal chemical alteration at the source, a similar conclusion to the CIA values obtained for Bradbury APXS analyses (McLennan et al., 2014; Hurowitz et al., 2017; Siebach et al., 2017). In contrast, constrained bulk rock analyses for the Mt Sharp Group have a relatively elevated average CIA value (52 ± 8) compared to Bradbury, though it is within error of Bradbury's average (Table 2). These similar averages suggest that the difference

in chemical weathering for constrained bulk rock analyses has not been strong for either stratigraphic group. However, average CIA values do vary between the different stratigraphic units and waypoints within the Bradbury and Mt Sharp Groups (Table 2). Notably, the coarser grained units (Glenelg, Gillespie Lake, Darwin and Kimberley) generally demonstrate higher CIA values, particularly Darwin (CIA 44 ± 8) compared to the fine-grained, mafic Sheepbed mudstone (CIA 40 ± 4). This difference may either reflect contributions from a relatively felsic sedimentary source region, or the mineral sorting regime preferentially preserving felsic minerals over mafic minerals in coarser grained units (Fedo et al., 2015; Siebach et al., 2017), as felsic material has a naturally higher CIA value compared to sediments rich in mafic minerals (Nesbitt and Wilson, 1992).

Previous CIA studies (Hurowitz et al., 2017; Siebach et al., 2017; Mangold et al., 2018) on Gale crater sediments have highlighted a variation between the Bradbury Group's Sheepbed Member mudstone and Mt Sharp Group's Murray formation mudstone. APXS analyses (Hurowitz et al., 2017; Siebach et al., 2017) and ChemCam analysis (Mangold et al., 2018) show the Mt Sharp Group to have notably higher CIA values compared to the Bradbury Group which has led these authors to hypothesise that Murray formation mudstones have undergone more chemical weathering at their source compared to Sheepbed Member mudstones. Our ChemCam analyses of the constrained bulk rock dataset also show Murray formation CIA values to be higher than those of the Sheepbed Member (Murray formation CIA = 51 ± 6 to 55 ± 5, Sheepbed Member = 40 ± 4; Table 2). Hurowitz et al. (2017) hypothesised that the differences in APXS derived CIA values between the Sheepbed (CIA 34 ± 2) and Murray Pahrump Hills (CIA 45 ± 4) mudstone units reflect modest, short-term paleoclimate fluctuations. According to Hurowitz et al. (2017), the Sheepbed mudstone sediments were eroded and transported during a colder, drier period compared to the Murray formation sediments, and that geochemical variation between these mudstone units is unlikely to be related to a different igneous source. The early stages of chemical weathering in basalts can liberate substantial amorphous silica from primary igneous phases which are susceptible to weathering (McLennan, 2003; Nesbitt and Wilson, 1992; McLennan et al., 2014). On this basis, Hurowitz et al. (2017) also associated the relatively elevated SiO_2 concentrations in the Murray formation with respect to Sheepbed mudstone as being caused by the greater degree of weathering, particularly as CIA and SiO_2 share a (weak) positive correlation between the two mudstone units for APXS analyses.

Fig. 10 shows calculated CIA values for our constrained ChemCam bulk rock dataset plotted against SiO_2, MgO and FeO_T. We also conducted SLR models of the mudstone dataset for SiO_2, MgO and FeO_T against CIA (Fig. 10; Appendix C). Our results show a minor ($r^2 = 25.5\%$), but statistically significant ($p < 0.05$) correlation between CIA and SiO_2 (Fig. 10A). This slight correlation suggests that chemical weathering may have somewhat increased SiO_2 concentrations between the Murray and Sheepbed mudstones (the model suggests an increase in 2.6 wt% SiO_2 for every 10% increase in CIA values) prior to Murray formation deposition, but in general the variation in SiO_2 concentrations cannot be explained by CIA values alone. In addition, the regression models show that neither MgO nor FeO_T present a significant correlation with CIA values (Fig. 10B, C). The FeO_T regression model does not show a statistically significant correlation with CIA, having high p-values ($p = 0.67$; Appendix Table C.3). On the other hand, modelled MgO concentrations do show a very weak negative correlation with CIA ($r^2 = 11.1\%$), for a p-value < 0.01 denoting statistical significance (Appendix Table C.2), though this still leaves most of the MgO variation between the mudstone units unaccounted for. Hence, chemical weathering does not appear to fully explain chemical differences between the Sheepbed and Murray mudstones. According to these models, the increased SiO_2, and decreased MgO present in the Mt Sharp Group is likely a factor of different source region geochemistry, and not sufficiently explained by different degrees of chemical weathering. Furthermore, the strong association of Na_2O with Al_2O_3 in both stratigraphic groups according to MLR and SLR models (Appendix B) suggests that feldspar is still the dominant control on this major element oxide across Gale samples.

The slightly elevated CIA values in the Murray formation mudstones must therefore be related to the lower CaO, and higher Al_2O_3 contents compared to Sheepbed. A decrease in CaO was also noted by Mangold et al. (2018) to be correlated with CIA within the Mt. Sharp Group members that were studied in that work. In the Sheepbed mudstones, CaO and Al_2O_3 have a Pearson correlation coefficient indicative of a strong correlation ($r = 0.60$; Appendix B), but these elements are poorly correlated in the Murray formation ($r = 0.23$). These correlation coefficients suggest that in the Sheepbed mudstone, CaO is present within Al-bearing mineral phases such as plagioclase feldspar and pigeonite – which is supported by CheMin derived mineral compositions (Morrison et al., 2018). Although Murray formation pigeonite determined by CheMin possesses little or no CaO, CaO was identified within the plagioclase feldspar component (Morrison et al., 2018). Hence, dissolution of plagioclase feldspar by chemical weathering at the source region or during transport may have liberated some Ca^{2+} and Al^{2+} cations into solution. The most common secondary minerals to form from the chemical weathering of basaltic minerals are smectites and kaolinites, both of which are associated with Al^{2+}, but neither smectites nor kaolinites incorporate significant (>3.5 wt%; Deer et al., 1992) Ca^{2+} into their crystal structure (Deer et al., 1992; Nesbitt and Wilson, 1992). This would result in some Ca^{2+} remaining in solution and being transported away from the system. As plagioclase feldspar is more resilient to chemical weathering than olivine and volcanic glass (Nesbitt and Wilson, 1992), it is likely that these will have also experienced some chemical weathering, liberating Mg and Fe ions into solution that could bond with Al to form Mg- and Fe-bearing smectites.

In addition to the relatively low CaO content in the Murray mudstones potentially relating to chemical

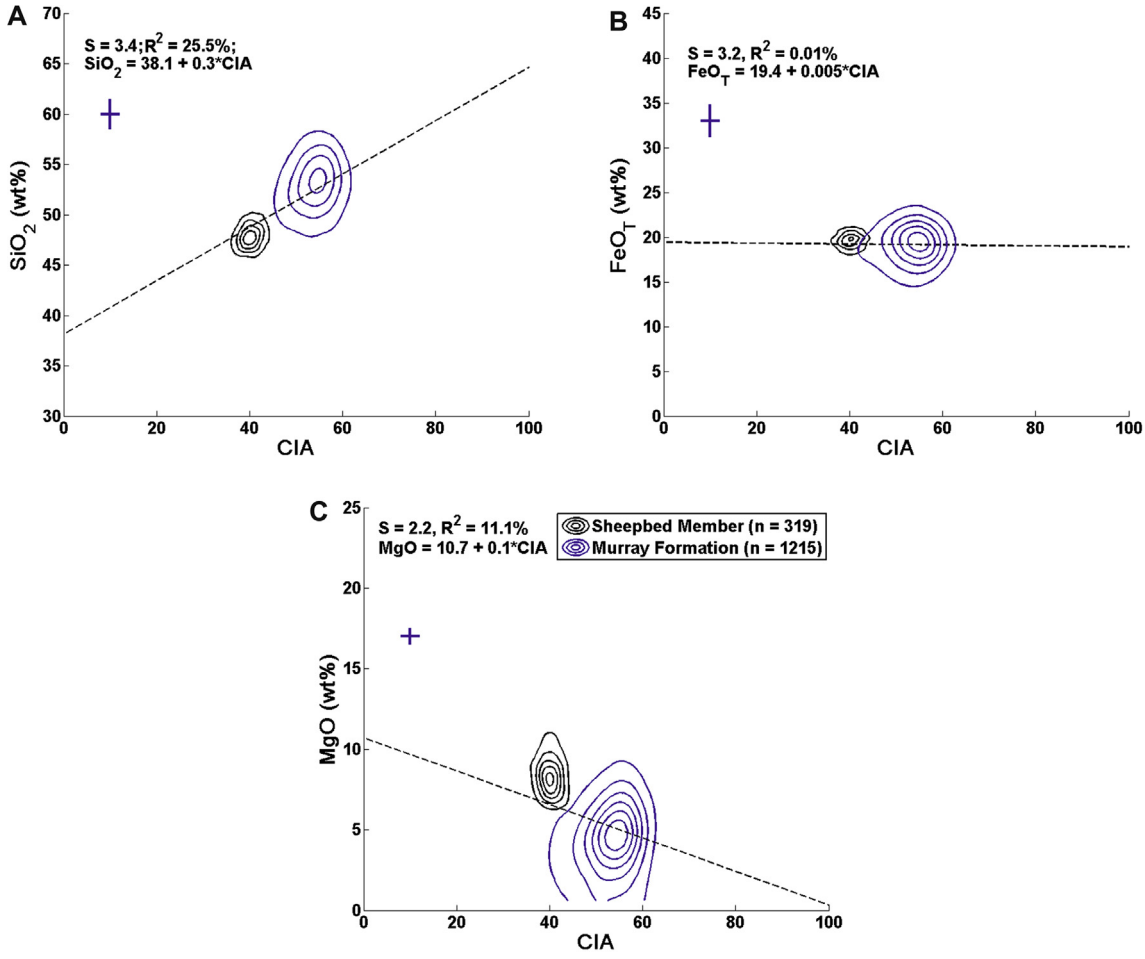

Fig. 10. Density contours of ChemCam observation point analyses from the Sheepbed Member and Murray Formation mudstone (excluding the Marias Pass area). These contours show A) SiO_2, B) MgO, and C) FeO_T, plotted against CIA values (see Table 2 for determination of CIA values). ChemCam precision is shown as the respective dark blue lines. The regression line (dashed black line) for the Linear Regression models (see Appendix C.2–C.4) were calculated using Minitab v17 to test the linear relationship of the Sheepbed and Murray formation mudstones.

weathering, the apparent lack of substantial CaO in Murray pigeonites may also be a product of relatively low CaO at the source. If the source of the Murray mudstones was richer in felsic material through a more evolved magmatic composition (indicated by the pigeonite's intermediate Fe/Mg ratio; Morrison et al., 2018), this would generate naturally higher CIA values than a more mafic source. In this scenario, these naturally higher CIA values may have been accentuated by minor chemical weathering, but not enough to drastically alter or mask source region characteristics. As the CIA values only show a weak correlation with SiO_2 and MgO, no correlation with FeO_T, and average Murray CIA values are not situated considerably above 50 – the CIA value of pure feldspar – we conclude that the degree of chemical weathering of Murray formation source material was not significant enough to mask source region characteristics in our constrained bulk rock dataset. Therefore, we favour that geochemical variation between the Sheepbed Member and Murray formation mudstones is more likely a factor of different source regions.

4.2. Variation of source region characteristics with grain size

4.2.1. Endmembers identified in the coarse-grained (>1 mm) units

Coarse-grained targets (Fig. 2; Le Deit et al., 2016; Mangold et al., 2016; Siebach et al., 2017) were identified within the Darwin Outcrop (sols 392–401), on the Kimberley to Darwin traverse (sols 401–574), at the Kimberley Waypoint (Point Coulomb, Jum Jum target and Liga Members; sols 574–632), and at the base of the Mt. Sharp Group at Pahrump Hills (Bald Mountain 1 and 2; sols 775–778). Bulk ChemCam observation point analyses for these pebbly units plot within the basalt to trachybasalt igneous float and clast density contours, and constitute the majority of point analyses in the Bradbury Group's high aluminium sub-focus (Figs. 11A, 12A). Total-alkali versus silica (TAS) plots are commonly applied to terrestrial magmatic rocks in order to distinguish the extent of fractionation that a magma has undergone (Le Bas et al., 1986). On Earth, geochemical variation of coarse sediments (grain size greater than 1 mm) is largely inherited from source rock

characteristics (Tolosana-Delgado and von Eynatten, 2009). At Gale crater, the number of igneous float and clasts identified within coarse-grained units and targets (Mangold et al., 2016; Edwards et al., 2017) suggests that this is also true for Gale's conglomerates. Due to the lack of large scale chemical remobilisation in the Bradbury Group and presence of primary igneous minerals (Fig. 9), this plot reveals likely detrital source compositions and geochemical differences between the groups relating to the alkali contents (Mangold et al., 2017b), especially when compared to the Gale crater igneous float and clasts. The distribution of igneous float rock and Bradbury Group density contour focal compositions are consistent with smoothed estimates of bulk rock compositions. The foci of the compositional contours for the Bradbury group and igneous float rocks are not coincident with the most abundant primary igneous minerals. Therefore, similar to the results of Cousin et al. (2017), this indicates that a mixture of minerals is analysed by ChemCam at most observation points, including for relatively coarse mineral grains.

Darwin-type conglomerate observation point analyses (Darwin and Darwin to Kimberley traverse analyses) are concentrated within the high-Al_2O_3 igneous float and Bradbury sub-focus (Fig. 11A), which make it likely that the coarse-sand matrix and small pebbles of Darwin-type conglomerates are derived from the trachybasalt parent rock. Meanwhile, the Kimberley-type conglomerates are relatively more enriched in K_2O than Darwin-type conglomerates (Figs. 11D and 12A) suggesting that a potassium-rich endmember has contributed to this stratigraphic unit (Le Deit et al., 2016). The potassium enrichment correlates with the presence of sanidine detected at high concentrations (~20%) in the Windjana drill hole within the Dillinger Member sandstone linked to a potassic-igneous source (Treiman et al., 2016). The JumJum conglomerate target (sol 550) representative of the lowermost Point Coulomb Member in the Kimberley formation also has elevated K_2O/Na_2O ratios. Hence, during the period of deposition in the sedimentary units leading up to Kimberley, this trachytic endmember grew in significance as a Gale source region (Le Deit et al., 2016).

Aside from source region variation of the sediments in Gale, an alternative hypothesis relating to Martian mineral sorting regimes could explain why both the igneous and high-aluminium Bradbury Group density contours are co-located between the alkali and plagioclase feldspar compositions (Figs. 11A, 12A). Feldspars have been noted to be more resilient to physical weathering than mafic minerals (Nesbitt and Young, 1996; Fedo et al., 2015), and hence are more concentrated in coarse-grained fluvial sediments

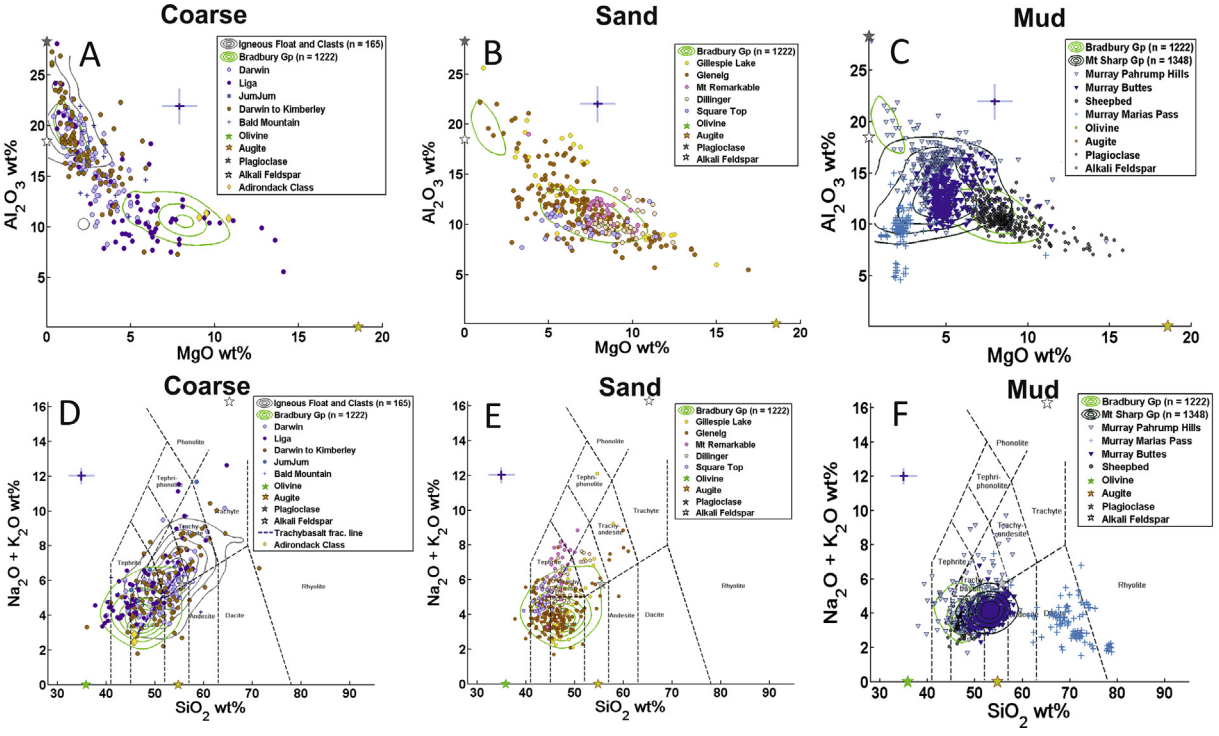

Fig. 11. ChemCam observation point analyses for Gale crater stratigraphic units and targets shown on Al_2O_3 versus MgO major oxide diagrams and total alkali-silica diagrams. Plots are displayed in accordance to the grain size fraction represented (left column is coarse (>1 mm), middle column sand grain (0.062–1 mm) and the right column is mud grain size (<0.062 mm). Igneous group contours are derived from Gale crater igneous float rocks and clasts data (Mangold et al., 2016; Edwards et al., 2017) and olivine fractionation line determined by Edwards et al (2017), CheMin derived Martian mineral compositions for the Rocknest (olivine, plagioclase, augite) and Windjana (alkali feldspar) samples are taken from Morrison et al. (2018), Adirondack Class basalt compositions (Gellert et al., 2006).

eroded from basaltic provenances (Siebach et al., 2017). The scatter of these observation point analyses towards modelled Gale feldspar compositions could suggest that the trachybasalt source signature identified in coarse sediments may be a result of the concentration of feldspar resulting from this Martian fluvial mineral sorting regime. However, as most conglomerate targets are poorly sorted, and have therefore been derived from multiple source rocks (Grotzinger et al., 2014, 2015), we favour the initial interpretation that the felsic nature of the coarse-grained units are considered to be representative of input from the trachybasalt source composition described by Edwards et al. (2017), and a potassic source described by Treiman et al. (2016) in the Kimberley formation Liga conglomerate Member.

4.2.2. Endmembers identified in the sandstone units (0.062–1 mm)

Fluvial sandstones are present within the Glenelg and Gillespie Lake Members of the Yellowknife Bay formation (Grotzinger et al., 2014; Anderson et al., 2015) as well as the Kimberley formation's Square Top, Dillinger, and Mt. Remarkable Members (Grotzinger et al., 2015; Treiman et al., 2016). On Earth, sandstones and shales have been related to source regions on the basis of their SiO_2/Al_2O_3 and Na_2O/K_2O ratios (Pettijohn et al., 1972; Roser and Korsch, 1986). They are also classified according to their relative abundances of quartz, feldspar and lithic fragments as these mineral populations are abundant in terrestrial sediments (Pettijohn et al., 1972; Dickinson, 1988; Weltje, 2012). On Mars, quartz has not been detected with CheMin at concentrations >1% (Fig. 9; Vaniman et al., 2014; Treiman et al., 2016; Rampe et al., 2017a; Yen et al., 2017), therefore the SiO_2/Al_2O_3 ratios employed by most terrestrial sediment geochemical classification schemes (Pettijohn et al., 1972; Herron, 1988) cannot distinguish key mixing components on Mars. Instead, due to the abundance of mafic minerals (especially clinopyroxene) detected in the CheMin analyses of drilled samples, we use the log-ratio $Al_2O_3/(MgO + FeO_T)$ to distinguish between these mafic and felsic contributions in sandstone and fine-grained units (Fig. 12D–F). The log-ratios FeO_T/K_2O (Fig. 12D–F) and K_2O/Na_2O (Fig. 12A–C and 13, plotted against SiO_2 to differentiate between possible igneous rock sources) are employed to distinguish volcanic lithic-fragments and feldspars from evolved (K-rich feldspar) and relatively primitive (Na-rich feldspar) sources.

The majority of Gale's sandstone compositions plot within the mafic Bradbury Group sub-focus, with some coarse sandstone units trending towards high-Al_2O_3 compositions (Fig. 11B). The low-Al_2O_3 sub-focus has a similar geochemical composition (though at face value is slightly more K_2O-rich and MgO-poor) compared to the tholeiitic Adirondack Class basalts sampled in Gusev crater by the MER *Spirit* rover (Fig. 11A and D). The Adirondack Class basalts are olivine-phyric, primitive basalts representative of primary, basaltic melt (Gellert et al., 2006; McSween et al., 2006; Filiberto et al., 2008; McCubbin et al., 2008). The similarity in composition between these and the majority of the Bradbury Group sediments indicates that Gale's dominant endmember composition is potentially derived from a comparable subalkaline basalt (Vaniman et al., 2014; Edwards et al., 2017). This subalkaline basalt endmember was also identified from ChemCam and CheMin analyses on fluvial sandstone (Treiman et al., 2016), and APXS analyses of Bradbury sediments (Siebach et al., 2017).

Sandstone units with grain size variation between coarse and fine sand (e.g., Glenelg; Anderson et al., 2015) demonstrate scatter that trends towards feldspar (Fig. 11B and E). Due to the poor to moderately sorted nature of the sandstone units (Grotzinger et al., 2014, 2015) the mafic-felsic mineral sorting regime outlined in Section 4.2 and described by Siebach et al. (2017) is also unlikely to have had a significant effect on sandstone compositions. Hence, this scatter may relate to sediment contribution from the trachybasalt endmember identified in the conglomerate units. However, as there is grain size variation within the units themselves, it is not clear to what extent the high proportion of plagioclase feldspar in this unit has been concentrated in the coarser fraction as a result of the mineral sorting regime (Siebach et al., 2017). Therefore, it is impossible to discern whether these feldspar-rich sediments were related to the trachybasalt source type or feldspar from the low-Al_2O_3, basaltic source that was concentrated in the coarser beds.

A clear difference can be seen between the Yellowknife Bay and Kimberley formation sandstones (Square Top, Dillinger and Mt. Remarkable Members) based on potassium-enrichment (Figs. 11E and 12B). The upper Dillinger and Mt. Remarkable Members are particularly distinct, forming their own cluster. As the CheMin analysis was conducted within the Dillinger Member, it can be assumed that the less K_2O-rich Square Top Member of the Kimberley formation contains a lower abundance of sanidine. The Glenelg and Gillespie Lake Members also possess higher K_2O/Na_2O ratios (cf. Anderson et al., 2015) than the sodic Darwin and Hummocky plains conglomerates. If this is attributed to relative proportions of potassic and sodic feldspars this suggests that these coarse sandstone units also contain some sanidine mineral grains. Therefore, the hypothesised potassic-igneous endmember has had an influence on Gale's sediment mineral assemblage throughout its depositional history. But, either due to a change in source region contribution, or increased sandstone maturity (Grotzinger et al., 2015; Treiman et al., 2016), this endmember is only seen to significantly contribute to the later Dillinger and Mt. Remarkable stratigraphic units.

In summary, the sandstone units within Gale crater are largely derived from a subalkaline basalt source, similar to the Adirondack Class basalts of Gusev crater, with a minor contribution from a potassic volcanic source (Treiman et al., 2016). Sediment contribution from the potassic volcanic source appears to increase from the Darwin waypoint to the Kimberley formation (Le Deit et al., 2016) where it is seen to strongly influence the geochemical composition of the Dillinger and Mt Remarkable Members. The trachybasalt endmember described by Edwards et al. (2017) may have also contributed to the sedimentary record within this

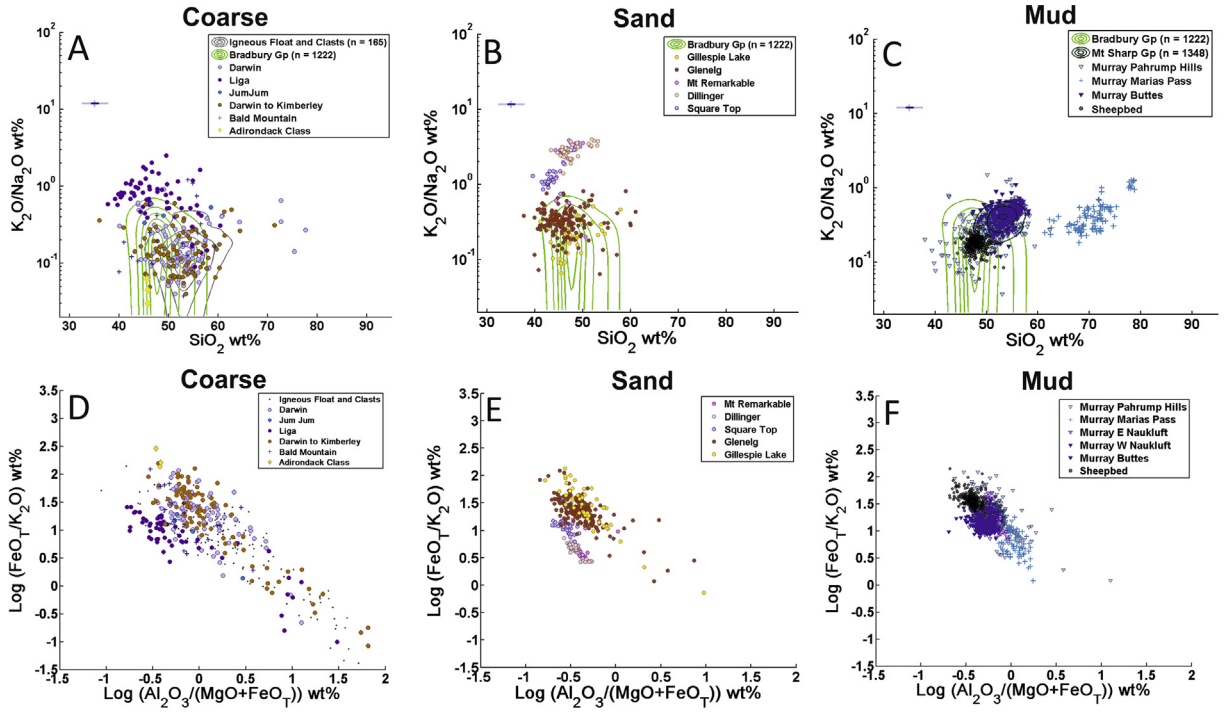

Fig. 12. ChemCam observation point analyses for Gale crater stratigraphic units and targets shown on K_2O/Na_2O against SiO_2 plots in order to distinguish potential differences in end member contributions (Roser and Korsch, 1986 and Adapted Herron (1988) log-ratio plot for sediments (see Section 4.2). Plots are displayed in accordance to the grain size fraction represented (left column is coarse (>1 mm), middle column sand grain (0.062–1 mm) and the right column is mud grain size (<0.062 mm). CheMin derived Martian mineral compositions for the Rocknest (olivine, plagioclase, augite) and Windjana (alkali feldspar) samples are taken from Morrison et al. (2018). Igneous group contours are derived from Gale crater igneous float rock and clast data (Mangold et al., 2016; Edwards et al., 2017).

grain size. However, it is not clear whether the increased abundance of feldspars present within these units are the result of the trachybasalt source region, or grain size variation within units.

4.2.3. Endmembers within the mudstone (<0.062 mm) units

The Sheepbed Member and Murray formation constitute Gale crater's mudstones (Grotzinger et al., 2014; Grotzinger et al., 2015). The vast majority of the Mt. Sharp Group's lower Murray formation possesses a relatively uniform composition throughout the East and West Naukluft, and Murray Buttes localities (Figs. 11 and 12). This general chemistry is more enriched in Al_2O_3, K_2O, SiO_2, and depleted in CaO, MgO, and Na_2O than the Sheepbed mudstone in the Bradbury Group (which plot within the mafic Bradbury contour focus). The very fine grain size of the Sheepbed mudstone and Murray formation results in more homogeneous compositions observed by ChemCam. Due to the removal of alteration features and targets potentially exposed to open system weathering (see methods Section 2.3, and Sections 3.2 and 4.1; Figs. 7–10), the observed geochemical variation between the Bradbury and Mt. Sharp Group (lower Murray) mudstone units must be representative of either lacustrine mineral sorting processes (Section 4.2.3.1), or different endmember mixing proportions (Section 4.2.3.2).

4.2.3.1. The effects of mineral sorting processes within the Gale lake on sediment geochemistry. A possible explanation for the observed geochemical differences between stratigraphic groups could relate to transport fractionation processes in a lake body. Supposing no change in sediment source region and assuming a homogeneous grain size of input materials, distal lake deposits will possess higher Al_2O_3 and alkali (especially Na_2O) concentrations due to greater, low density felsic and possibly clay-rich mineral abundances (Das et al., 2006; Jin et al., 2006; Babechuk et al., 2014). For Gale crater's Sheepbed mudstone, bed thicknesses and close association with overlying fluvial sandstone have been interpreted as a depositional environment that was relatively rapid, close to the shoreline and sediment source (McLennan et al., 2014; Hurowitz et al., 2017). It has also been argued by Hurowitz et al. (2017) that hematite-bearing sections of the Murray formation such as the Pahrump Hills were deposited in shallow water potentially near the shoreline due to high abundances of hematite and Mn-oxide pertaining to an oxidising environment. Trough cross-bedding and interstratified siltstone and fine sandstone near Pahrump also support deposition in shallower waters and/or proximity to the lake shoreline (Hurowitz et al., 2017). Therefore, if both the Sheepbed Member and Pahrump Hills Murray formation mudstones are deposited at near-shore locations in the paleolake, their differences in mineralogy and chemistry must reflect a change in source regions. The Pahrump Hills mudstones located near the interfingering boundary with the Bradbury Group are more Na_2O- and K_2O-rich, and possess greater abundances of plagioclase feldspar than the Sheepbed

mudstone (Figs. 9 and 12F) which is not what we would expect based on mineral density and sediment sorting alone.

In contrast, Rampe et al. (2017a) noted that the observed secondary mineral assemblages in Pahrump Hills that Hurowitz et al. (2017) attributes to a shallow lake environment could also be produced through diagenesis in short-lived, oxidizing ground waters. However, the morphological evidence for shallower lake conditions for the Mt Sharp Group near Pahrump is significant (thicker laminations, interstratified, cross-bedded, fine sandstones; Grotzinger et al., 2015; Hurowitz et al., 2017). Thus differing source regions between the Murray formation and Sheepbed Member mudstones are the most plausible explanation for their compositional differences.

4.2.3.2. Endmembers and source region contributions. In this section we build on the model above that chemical weathering in source materials, diagenesis and transport processes have not erased the source rock compositions of the mudstones. The Sheepbed Member consistently plots within the dominant, Mg-rich focal composition of the Bradbury Group (Figs. 11C, F, 12C) and is similar in composition to the Adirondack Class basalts and subalkaline basalt endmember determined by Edwards et al. (2017) from Gale crater's igneous pebbles and float (Fig. 11C). Therefore, the Sheepbed mudstone unequivocally relates to the dominant, subalkaline basalt source region that has also contributed sediment to the Bradbury Group's sandstones and conglomerates. In contrast, the Mt Sharp Group MgO composition appears intermediate between those of the Bradbury trachybasalt and subalkaline basalt subfocal compositions (Figs. 6D and 11C) suggesting similar mixing between a mafic and felsic source. However, the increased K_2O, $Al_2O_3/(MgO + FeO_T)$ and SiO_2 content of the Murray formation compared to the Sheepbed mudstones (Figs. 11C, F, 12C, and F) requires a greater contribution of felsic minerals and silica-rich material. CheMin analyses (Fig. 9) also demonstrate this greater felsic/mafic mineral proportion.

CheMin XRD analyses show sanidine across the Murray formation (except for Mojave 2 and Oudam) with between 4.2% at the Buckskin drill hole, to 7.7% in Marimba 2 (Morris et al., 2016; Rampe et al., 2017b). These are higher abundances than those of sanidine detected in the Yellowknife Bay formation (2.9–3.4%). On average, Murray alkali feldspars are inferred to possess higher potassium content, more similar to that analysed at The Kimberley (Treiman et al., 2016; Rampe et al., 2017a). This suggests that the potassic igneous source identified in the Kimberley sandstone by Treiman et al. (2016) is likely a volumetrically significant contributor to Gale's sedimentary record. Though the presence of the potassic igneous endmember may explain some of the elevated potassium contents, it does not fully explain the increase in SiO_2 content for Murray. Hence, for the Mt. Sharp Group to be more silica and potassium enriched – elements not commonly seen on Earth to change significantly with increased lake depth for sediments derived from the same source region (Das et al., 2006; Jin et al., 2006) – we infer, based on our analysis above, the presence of a distinct source region.

On Earth, tholeiitic terrains such as the Eastern Volcanic Zone of Iceland are usually punctuated by periods of silica-rich tholeiitic volcanism (Jakobsson, 1972; Bindeman et al., 2006; Haddadi et al., 2015). These silicic-tholeiites are derived from the fractionation of olivine-normative parent magmas at shallow or mid crustal depths (less than 15 km) within the crust (Green et al., 1967; Haddadi et al., 2015). All CheMin analyses in the Murray formation have notable silica-enrichment in the amorphous component (Morris et al., 2016; Rampe et al., 2017a), which may be volcanic glass or an alteration product thereof (Bish et al., 2013; Blake et al., 2013; Dehouck et al., 2014; Achilles et al., 2017; Rampe et al., 2017a). Terrestrial silicic-tholeiites also possess a slightly higher bulk K_2O content than olivine-tholeiites (Green et al., 1967; Bindeman et al., 2006). Along the rover traverse the K_2O content is seen to increase with silica from the Pahrump Hills to the Murray Buttes area (Fig. 12C; excluding the Marias Pass silica-rich area). CheMin-determined pigeonite compositions for the Murray formation are also very low in calcium and possess intermediate Fe/Mg (Rampe et al., 2017a; Morrison et al., 2018). The latter characteristic especially is the hallmark of a more fractionated, magma source (Deer et al., 1992).

Though not seen throughout the Mt. Sharp stratigraphy, tridymite and cristobalite were detected in abundance at Marias Pass (Morris et al., 2016), and cristobalite in abundance in Telegraph Peak (Rampe et al., 2017a). These minerals are high temperature, low pressure silica polymorphs (Shinohara and Kohyama, 2004) that usually form within late-stage, strongly-fractionated magmas on Earth (Keith and Muffler, 1978; Morris et al., 2016). Marias Pass mudstone thus shows influence by a completely distinct source region not detected in the Bradbury Group, and provides strong evidence for a temporally evolving sediment composition. Marias Pass sediments appear derived from a highly fractionated, silica-rich ($\geq$75 wt% SiO_2) endmember which contributed the tridymite and cristobalite. This region also contains a continued – but minor – influence of the potassic endmember (Figs. 9 and 12C). The extreme low density of these silica polymorphs (2.3 g/cm^3) and the fine-grained nature of the material (e.g., Frydenvang et al., 2017) means that this endmember could be located far from the Gale crater catchment area, allowing them to be entrained longer in the fluid flow transport. With more time spent in the fluid flow, mineral sorting will have had a greater effect resulting in the concentration of these endmember mineral grains along with fine-grained amorphous material or detrital clays, at the end of the distributary system. However, aqueous alteration models (i.e., Bridges et al., 2015), and the lack of clays in the Telegraph Peak and Buckskin drill holes suggest that Gale's clay component is primarily authigenic. Concentration due to density-related transport fractionation could explain the localised high abundance of tridymite along with significant amorphous content (60%, Morris et al., 2016) identified by CheMin at the Buckskin drill hole (sol 1061).

Alternative explanations have been proposed by others to explain the presence of the high-silica Marias Pass unit. The first suggests that it was deposited in a temporally isolated event, such as a relatively sudden, volcanic eruption of a highly evolved silicic magma (Morris et al., 2016). This could have generated a thick layer of ash that was later washed downstream into the lake (Morris et al., 2016). Once this eruption had ceased, a return to the mafic sediments deposited prior to the eruption occurred, resulting in the distinct Marias Pass stratigraphic unit within the Murray formation (Morris et al., 2016; Frydenvang et al., 2017). The second explanation for silica-enrichment in Marias Pass discusses that sediments may have been leached in place by short-lived, mildly acidic, late-stage fluids (Rampe et al., 2017a). These diagenetic fluids could have dissolved ferromagnesian minerals and created the observed trace element trends (Rampe et al., 2017a). As tridymite is strongly inferred to be detrital from a silicic source region (Morris et al., 2016), and as the abundance of magnetite and lack of hematite at this locality is more indicative of reducing settings (Hurowitz et al., 2017), we prefer a source region and deposition-related hypothesis to explain the presence of this unusual unit.

5. CONCLUSIONS

Investigation of the ChemCam database from the beginning of the mission through to sol 1482 suggests that the main influences on observed geochemical variation are changing sediment sources (see Table 3 for endmember compositions), and mineral sorting regimes once diagenetic features are removed from the database and the effects of chemical weathering have been taken into account. The dominance of primary igneous minerals, and CIA values unrelated to SiO_2 and MgO variations in our constrained dataset, all suggest that chemical weathering processes have not dominated the endmember compositions despite CIA values being higher in the Mt Sharp Group mudstones compared to the Sheepbed mudstone Member. Instead, bulk compositions for the stratigraphic units and groups are likely determined by varying proportions of primary igneous minerals, with isochemical weathering hypothesised to generate amorphous and phyllosilicate component compositions similar to bulk rock geochemistry. Our results also support the Martian fluvial mineral sorting regime whereby felsic minerals are more abundant in coarse sandstone fractions due to their resilience to diminution during transportation (Siebach et al., 2017), but are more likely to travel farther into a lake body because of their lower density compared to mafic minerals. As a consequence of the Murray formation and Sheepbed mudstone possessing a possibly similar depositional setting in relatively shallow water and/or close to the shoreline, the compositional differences between these units likely reflect changes in sediment source region. This change in sediment provenance is particularly notable in the Marias Pass region with the appearance of the silica-rich endmember and we propose a silica-rich, subalkaline basalt endmember to be the main source of sediments at the base of Mt Sharp.

In isolating the analysis to grain size dependent subpopulations, four previously identified endmembers and one new endmember are observed throughout Gale crater sediments in this part of the mission, which can be related to specific igneous source regions (Fig. 13). These are:

1. A subalkaline basalt endmember (Anderson et al., 2015; Siebach et al., 2017); similar in composition to the Adirondack Class basalts observed by the MER *Spirit* rover at Gusev. This endmember is observed throughout the Bradbury Group stratigraphy and is concentrated within the Sheepbed mudstone Member of Yellowknife Bay. Due to the similarity of this composition to Adirondack basalts it can be inferred that this is most likely a regional endmember composition and contributes significantly to Gale's geochemical record.
2. A trachybasalt endmember (Edwards et al., 2017); likely formed during crystal-melt fractionation of the mafic, Adirondack-type basalt that constitutes endmember (1). This is largely identified in clasts within the conglomerate outcrops (especially Darwin), and is characterised by Na_2O and Al_2O_3 enrichment associated with an increase in plagioclase feldspars.
3. A trachyte endmember (Treiman et al., 2016); related to an increased abundance of sanidine in comparison to the more Na-rich plagioclase feldspars from endmember (2). This endmember is recognised to an extent within the Gillespie Lake and Glenelg Members of the Yellowknife Bay formation, plus the later Mt. Sharp Group mudstone. It is seen to contribute significantly to the Kimber-

Table 3
A table of the ChemCam derived sediment endmember compositions in Gale crater from this study and Edwards et al. (2017). Propagated 1σ error is provided in brackets for the modelled endmember compositions. Exact compositions cannot be derived from bulk sediment analysis for the trachyte and rhyolite endmembers as these are based on the presence of specific minerals within complex sedimentary units that were either derived from multiple igneous source regions (i.e., Windjana sandstone, Treiman et al., 2016) or have experienced uncertain levels of aqueous alteration (i.e., the Marias Pass mudstones, Frydenvang et al., 2017).

Endmember	SiO_2	TiO_2	Al_2O_3	FeO_T	MgO	CaO	Na_2O	K_2O	Reference
Subalkaline	47.4	0.9	10.6	19.8	8.1	5.5	3.0	0.5	This paper, Edwards et al.
Basalt	± 1.4	± 0.2	± 1.2	± 1.9	± 0.9	± 1.6	± 1.4	± 0.3	(2017)
Trachybasalt	55.2	0.8	19.8	7.7 ± 5.6	1.6	6.4	5.4	1.2	Edwards et al. (2017)
	± 3.5	± 0.2	± 2.5		± 1.0	± 2.4	± 1.3	± 0.9	
Silica-rich	53.1	1.0	12.1	19.5	4.6	2.3	2.9	1.2	This paper
Basalt	± 1.9	± 0.2	± 0.8	± 1.4	± 0.6	± 0.6	± 0.2	± 0.2	

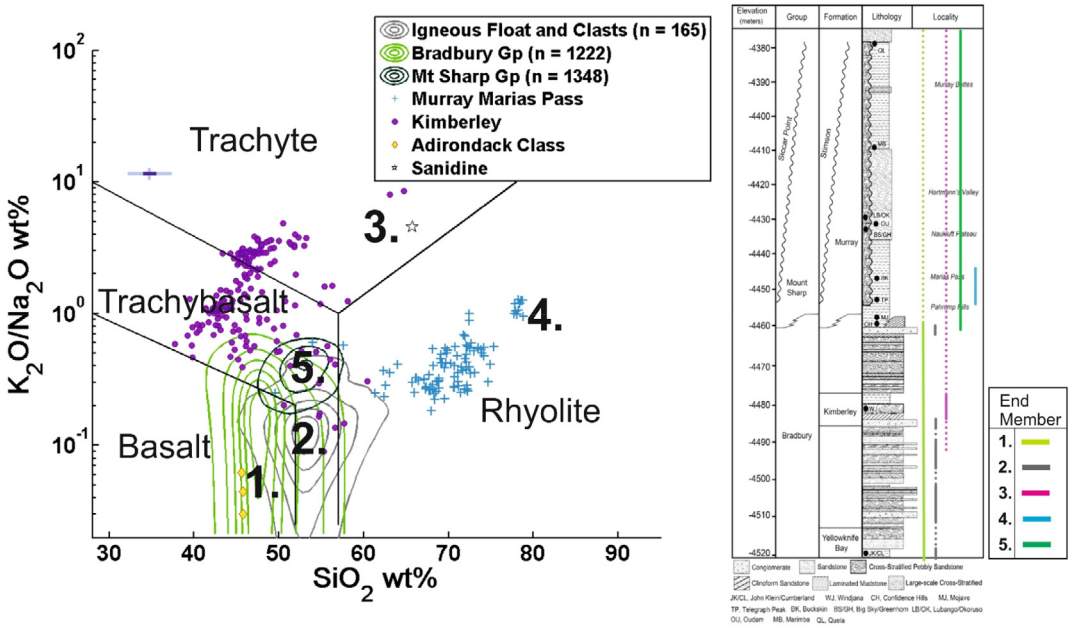

Fig. 13. A K_2O/Na_2O vs SiO_2 plot of stratigraphic units most influenced by unique endmembers alongside the Gale crater stratigraphic column, modified to show approximately where each end member is predicted to contribute to the stratigraphic record. Field boundaries of sediment source regions for the K_2O/Na_2O vs SiO_2 plot are determined by replotting the basalt, trachybasalt, trachyte, and rhyolite TAS silica field boundaries (Le Bas et al., 1986) against terrestrial basalt, trachybasalt, trachyte, and rhyolite compositions obtained from the georoc.de database. Derived endmembers are 1. Adirondack-type subalkaline basalt which constitutes the majority of the Bradbury group sediment compositions, and is the most dominant throughout the stratigraphic succession (light green line). 2. A trachybasalt endmember largely recognised in the coarse-grained conglomerate and sandstone units (grey line), 3. A potassium-rich (trachyte) volcanic source region, which is largely expressed in the Kimberley formation sandstones (pink line), 4. A silica-rich (rhyolite) volcanic endmember, most dominant in the Marias Pass locality of the Mt Sharp Group (light blue line), and 5. A silica-rich subalkaline basalt endmember composition present in the Mt Sharp group Murray mudstones (dark green line). Adirondack Class basalt compositional data are also displayed (Gellert et al., 2006). Dashed lines on the stratigraphic column show where the endmember contributes to a lesser extent, undashed lines show the endmembers that are most dominant in that stratigraphic area. (For interpretation of the references to colour in this figure legend, the reader is referred to the web version of this article.)

ley formation sandstones and conglomerates and – due to the detected sanidine being of a high order – it may be associated with erosion from a volcanic alkaline or trachytic source (Treiman et al., 2016).

4. A silica-rich (rhyolite) igneous endmember (Morris et al., 2016); identified at the Marias Pass locality within the Mt. Sharp Group, this endmember is thought to resemble the erosion of a late-stage magmatic source, or ash cloud generated from a volcanic event of an evolved magma composition, due to the predominance of high-temperature silica polymorphs.
5. A silica-rich, subalkaline basaltic endmember; proposed by this study, this endmember contributes most to the Mt. Sharp Group and is more SiO_2, Al_2O_3 and K_2O-rich than endmember (1). This endmember is seen to become more prevalent up the stratigraphic succession.

The above source compositions have strongly influenced the geochemistry and mineralogy of the sedimentary rocks which constitute the Bradbury and Mt. Sharp (Murray formation up to sol 1482) fluviolacustrine stratigraphic groups traversed by MSL. Endmembers (1) and (2) are largely associated with the distal alluvial fan deposits seen within the Bradbury Group (Grotzinger et al., 2014; Grotzinger et al., 2015) while endmembers (4) and (5) are solely recognised in the lower Murray formation. Endmember (3) is identified across the fluviolacustrine deposits, predominately in Bradbury Group fluvial sandstone and Murray mudstone, but contributes little to the Yellowknife bay formation. Instead, the Yellowknife bay formation appears to be largely derived from endmember (1) with some local influence of endmember (2).

This study shows that despite temporal and spatial influences on sediments, unique source region characteristics can still be distinguished within the Martian sedimentary record. This can be achieved through identifying chemical and mineralogical trends that contradict physical sorting processes, as well as analysing sediments according to grain size. Gale crater stratigraphy therefore shows that the ancient highland crust which contributed to its basin fill is more geochemically complex than previously anticipated for Mars. This is despite the lack of evidence for evolved crustal compositions detected from orbit which we speculate may relate to evolved rocks being volumetrically smaller relative to basalt in Mars' crust.

ACKNOWLEDGMENTS

CCB was supported through the RCUK STFC Open 2015 DTP doctoral training grant (ST/N50421X/1) to the OU. JCB and SPS were supported through a UKSA grant (ST/P002110/1). JF thanks

the Calsberg Foundation for support. The MSL engineering, ChemCam, CheMin and science teams are gratefully acknowledged for the acquisition of the data used in this paper. Support for this work in the US is provided by the NASA Mars Exploration Program. The authors would also like to thank Kirsten Siebach for her comments on the manuscript. This work was improved by comments from three anonymous reviewers on an earlier version of this manuscript.

APPENDICES A–D. SUPPLEMENTARY MATERIAL

Supplementary data to this article can be found online at https://doi.org/10.1016/j.gca.2018.11.031.

REFERENCES

Achilles C. N., Downs R. T., Ming D. W., Rampe E. B., Morris R. V., Treiman A. H., Morrison S. M., Blake D. F., Vaniman D. T., Ewing R. C., Chipera S. J., Yen A. S., Bristow T. F., Ehlmann B. L., Gellert R., Hazen R. M., Fendrich K. V., Craig P. I., Grotzinger J., Des Marais D. J., Farmer J. D., Sarrazin P. C. and Morookian J.-M. (2017) Mineralogy of an active eolian sediment from the namib dune, Gale crater, Mars. *J. Geophys. Res. Planets* **122**, 2344–2361. https://doi.org/10.1002/2017JE005262.

Agee C. B., Wilson N. V., McCubbin F. M., Ziegler K., Polyak V. J., Sharp Z. D., Asmerom Y., Nunn M. H., Shaheen R., Thiemens M. H., Steele A., Fogel M. L., Bowden R., Glamoclija M., Zhang Z. and Elardo S. M. (2013) Unique meteorite from early amazonian mars: water-rich basaltic breccia northwest Africa 7034. *Science* **339**, 780–785. https://doi.org/10.1126/science.1228858.

Anderson R. B., Clegg S. M., Frydenvang J., Wiens R. C., McLennan S., Morris R. V., Ehlmann B. and Dyar M. D. (2017) Improved accuracy in quantitative laser-induced breakdown spectroscopy using sub-models. *Spectrochim. Acta, Part B* **129**, 49–57. https://doi.org/10.1016/j.sab.2016.12.002.

Anderson R., Bridges J. C., Williams A., Edgar L., Ollila A., Williams J., Nachon M., Mangold N., Fisk M., Schieber J., Gupta S., Dromart G., Wiens R. C., Le Mouélic S., Forni O., Lanza N., Mezzacappa A., Sautter V., Blaney D., Clark B. C., Clegg S., Gasnault O., Lasue J., Leveille R., Lewin E., Lewis K. W., Maurice S., Newsom H., Schwenzer S. P. and Vaniman D. (2015) ChemCam results from the Shaler outcrop in Gale crater, Mars. *Icarus* **249**, 2–21. https://doi.org/10.1016/j.icarus.2014.07.025.

Archer P. D., Franz H. B., Sutter B., Arevalo R. D., Coll P., Eigenbrode J. L., Glavin D. P., Jones J. J., Leshin L. A., Mahaffy P. R., McAdam A. C., McKay C. P., Ming D. W., Morris R. V., Navarro-González R., Niles P. B., Pavlov A., Squyres S. W., Stern J. C., Steele A. and Wray J. J. (2014) Abundances and implications of volatile-bearing species from evolved gas analysis of the Rocknest aeolian deposit, Gale Crater, Mars. *J. Geophys. Res. Planets* **119**, 237–254. https://doi.org/10.1002/2013JE004493.

Babechuk M. G., Widdowson M. and Kamber B. S. (2014) Quantifying chemical weathering intensity and trace element release from two contrasting basalt profiles, Deccan Traps, India. *Chem. Geol.* **363**, 56–75.

Bandfield J. L. (2006) Extended surface exposures of granitoid compositions in Syrtis MajorMars. *Geophys. Res. Lett.* **33**, L06203. https://doi.org/10.1029/2005GL025559.

Bandfield J. L., Hamilton V. E. and Christensen P. R. (2000) A global view of Martian surface compositions from MGS-TES. *Science* **287**, 1626–1630. https://doi.org/10.1126/science.287.5458.1626.

Bandfield J. L., Hamilton V. E., Christensen P. R. and McSween H. Y. (2004) Identification of quartzofeldspathic materials on Mars. *J. Geophys. Res. Planets* **109**, E10009.

Banham S. G., Gupta S., Rubin D. M., Watkins J. A., Sumner D. Y., Edgett K. S., Grotzinger J. P., Lewis K. W., Edgar L. A., Stack-Morgan K. M., Barnes R., Bell J. F., Day M. D., Ewing R. C., Lapotre M. G. A., Stein N. T., Rivera-Hernandez F. and Vasavada A. R. (2018) Ancient Martian aeolian processes and palaeomorphology reconstructed from the Stimson formation on the lower slope of Aeolis Mons, Gale crater, Mars. *Sedimentology* **65**, 993–1042. https://doi.org/10.1111/sed.12469.

Bibring J.-P., Langevin Y., Mustard J. F., Poulet F., Arvidson R., Gendrin A., Gondet B., Mangold N., Pinet P. and Forget F. (2006) Global mineralogical and aqueous Mars history derived from OMEGA/Mars Express data. *Science* **312**, 400–404. https://doi.org/10.1126/science.1122659.

Bindeman I. N., Sigmarsson O. and Eiler J. (2006) Time constraints on the origin of large volume basalts derived from O-isotope and trace element mineral zoning and U-series disequilibria in the Laki and Grímsvötn volcanic system. *Earth Planet. Sci. Lett.* **245**, 245–259.

Bish D. L., Blake D., Vaniman D. T., Chipera S. J., Morris R. V., Ming D. W., Treiman A. H., Sarrazin P., Morrison S. M. and Downs R. T. (2013) X-ray diffraction results from mars science laboratory: mineralogy of rocknest at Gale crater. *Science* **341**, 1238932. https://doi.org/10.1126/science.1238932.

Blake D. F., Morris R. V., Kocurek G., Morrison S., Downs R., Bish D., Ming D., Edgett K., Rubin D., Goetz W., Madsen M. B., Sullivan R., Gellert R., Campbell J. L., Treiman A. H., McLennan S. M., Yen A. S., Grotzinger J., Vaniman D., Chipera S. J., Achilles C., Rampe E. B., Sumner D., Meslin P. Y., Maurice S., Forni O., Gasnault O., Fisk M., Schmidt M. E., Mahaffy P., Leshin L. A., Glavin D., Steele A., Freissinet C., Navarro-Gonzalez R., Yingst A., Kah L. C., Bridges N., Lewis K., Bristow T. F., Farmer J., Crisp J. A., Stolper E., Des Marais D. and Sarrazin P. (2013) Curiosity at Gale crater, Mars: characterization and analysis of the Rocknest sand shadow. *Science* **341**, 1239505. https://doi.org/10.1126/science.1239505.

Blaney D. L., Wiens R. C., Maurice S., Clegg S., Anderson R. B., Kah L. C., Le Mouélic S., Ollila A., Bridges N. and Tokar R. (2014) Chemistry and texture of the rocks at Rocknest, Gale crater: evidence for sedimentary origin and diagenetic alteration. *J. Geophys. Res. Planets* **119**, 2109–2131. https://doi.org/10.1002/2013JE004590.

Bloemsma M. R., Zabel M., Stuut J. B. W., Tjallingii R., Collins J. A. and Weltje G. J. (2012) Modelling the joint variability of grain size and chemical composition in sediments. *Sed. Geol.* **280**, 135–148. https://doi.org/10.1016/j.sedgeo.2012.04.009.

Bridges J. C., Hicks L. J. and Treiman A. H. (2019) Chapter 5 – carbonates on mars. In *Volatiles in the Martian Crust* (eds. J. Filiberto and S. P. Schwenzer). Elsevier, pp. 89–118.

Bridges J. C., Schwenzer S. P., Leveille R., Westall F., Wiens R. C., Mangold N., Bristow T., Edwards P. and Berger G. (2015) Diagenesis and clay mineral formation at Gale crater, Mars. *J. Geophys. Res. Planets* **120**, 1–19. https://doi.org/10.1002/2014JE004757.

Bristow T. F., Blake D. F., Vaniman D. T., Chipera S. J., Rampe E. B., Grotzinger J. P., McAdam A. C., Ming D. W., Morrison S. M. and Yen A. S. (2017) Surveying clay mineral diversity in the murray formation, Gale crater, Mars. *48th Lunar and Planetary Science, Houston, TX, United States*.

Bristow T. F., Bish D. L., Vaniman D. T., Morris R. V., Blake D. F., Grotzinger J. P., Rampe E. B., Crisp J. A., Achilles C. N., Ming D. W., Ehlmann B. L., King P., Bridges J., Eigenbrode J. L., Sumner D., Chipera S. J., Morookian J. M., Treiman A. H., Morrison S. M., Downs R. T., Farmer J., Des Marais D., Sarrazin P., Floyd M. M., Mishna M. and McAdam A. (2015) The origin and implications of clay minerals from Yellowknife Bay, Gale crater, Mars. *Am. Mineral.* **100**, 824–836. https://doi.org/10.2138/am-2015-5077CCBYNCND.

Calef F., Dietrich W., Edgar L., Farmer J., Fraeman A., Grotzinger J., Palucis M., Parker T., Rice M. and Rowland S. (2016) Geologic mapping of the mars science laboratory landing ellipse. *Ann. Planet. Geol. Mappers Meet.*.

Chevrier V. and Mathé P. (2007) Mineralogy and evolution of the surface of Mars: a review. *Planet. Space Sci.* **55**, 289–314. https://doi.org/10.1016/0160-9327(96)10013-2.

Chipera S. J. and Bish D. L. (2002) FULLPAT: a full-pattern quantitative analysis program for X-ray powder diffraction using measured and calculated patterns. *J. Appl. Crystallogr.* **35**, 744–749. https://doi.org/10.1107/S0021889802017405.

Chipera S. J. and Bish D. L. (2013) Fitting full X-ray diffraction patterns for quantitative analysis: a method for readily quantifying crystalline and disordered phases. *Adv. Mater. Phys. Chem.* **3**, 47. https://doi.org/10.4236/ampc.2013.31A007.

Christensen P. R., Bandfield J. L., Hamilton V. E., Ruff S. W., Kieffer H. H., Titus T. N., Malin M. C., Morris R. V., Lane M. D., Clark R. L., Jakosky B. M., Mellon M. T., Pearl J. C., Conrath B. J., Smith M. D., Clancy R. T., Kuzmin R. O., Roush T., Mehall G. L., Gorelick N., Bender K., Murray K., Dason S., Greene E., Silverman S. and Greenfield M. (2001) Mars global surveyor thermal emission spectrometer experiment: investigation description and surface science results. *J. Geophys. Res. Planets* **106**, 23823–23871. https://doi.org/10.1029/2000JE001370.

Clegg S. M., Wiens R. C., Anderson R., Forni O., Frydenvang J., Lasue J., Cousin A., Payré V., Boucher T. and Dyar M. D. (2017) Recalibration of the Mars Science Laboratory ChemCam instrument with an expanded geochemical database. *Spectrochim. Acta, Part B* **129**, 64–85. https://doi.org/10.1016/j.sab.2016.12.003.

Cousin A., Sautter V., Payré V., Forni O., Mangold N., Gasnault O., Le Deit L., Johnson J., Maurice S. and Salvatore M. (2017) Classification of igneous rocks analyzed by ChemCam at Gale crater, Mars. *Icarus* **288**, 265–283. https://doi.org/10.1016/j.icarus.2017.01.014.

Das B. K., Al-Mikhlafi A. S. and Kaur P. (2006) Geochemistry of Mansar Lake sediments, Jammu, India: implication for source-area weathering, provenance, and tectonic setting. *J. Asian Earth Sci.* **26**, 649–668. https://doi.org/10.1016/j.jseaes.2005.01.005.

Deer W. A., Howie R. A. and Zussman J. (1992) An Introduction to the Rock-Forming Minerals. Longman London.

Dehouck E., McLennan S. M., Meslin P.-Y. and Cousin A. (2014) Constraints on abundance, composition, and nature of X-ray amorphous components of soils and rocks at Gale crater, Mars. *J. Geophys. Res. Planets* **119**, 2640–2657. https://doi.org/10.1002/2014JE004716.

Dickinson W. R. (1988) Provenance and sediment dispersal in relation to paleotectonics and paleogeography of sedimentary basins. *New perspectives in basin analysis*, 3–25.

Edgett K. S., Yingst R. A., Ravine M. A., Caplinger M. A., Maki J. N., Ghaemi F. T., Schaffner J. A., Bell J. F., Edwards L. J., Herkenhoff K. E., Heydari E., Kah L. C., Lemmon M. T., Minitti M. E., Olson T. S., Parker T. J., Rowland S. K., Schieber J., Sullivan R. J., Sumner D. Y., Thomas P. C., Jensen E. H., Simmonds J. J., Sengstacken A. J., Willson R. G. and Goetz W. (2012) Curiosity's Mars Hand Lens Imager (MAHLI) Investigation. *Space Sci. Rev.* **170**, 259–317. https://doi.org/10.1007/s11214-012-9910-4.

Edwards P. H., Bridges J. C., Wiens R., Anderson R., Dyar D., Fisk M., Thompson L., Gasda P., Filiberto J., Schwenzer S. P., Blaney D. and Hutchinson I. (2017) Basalt–trachybasalt samples in Gale crater, Mars. *Meteorit. Planet. Sci.* **52**. https://doi.org/10.1111/maps.12953, 2931-2410.

Ehlmann B. L., Berger G., Mangold N., Michalski J. R., Catling D. C., Ruff S. W., Chassefière E., Niles P. B., Chevrier V. and Poulet F. (2013) Geochemical consequences of widespread clay mineral formation in Mars' ancient crust. *Space Sci. Rev.* **174**, 329–364.

Ehlmann B. L., Mustard J. F., Murchie S. L., Poulet F., Bishop J. L., Brown A. J., Calvin W. M., Clark R. N., Marais D. J. D., Milliken R. E., Roach L. H., Roush T. L., Swayze G. A. and Wray J. J. (2008) Orbital identification of carbonate-bearing rocks on mars. *Science* **322**, 1828–1832. https://doi.org/10.1126/science.1164759.

Eilers P. H. C. and Goeman J. J. (2004) Enhancing scatterplots with smoothed densities. *Bioinformatics* **20**, 623–628. https://doi.org/10.1093/bioinformatics/btg454.

Fedo C. M., McGlynn I. O. and McSween H. Y. (2015) Grain size and hydrodynamic sorting controls on the composition of basaltic sediments: implications for interpreting martian soils. *Earth Planet. Sci. Lett.* **423**, 67–77. https://doi.org/10.1016/j.epsl.2015.03.052.

Filiberto J., Treiman A. H. and Le L. (2008) Crystallization experiments on a Gusev Adirondack basalt composition. *Meteorit. Planet. Sci.* **43**, 1137–1146. https://doi.org/10.1111/j.1945-5100.2008.tb01118.x.

Filiberto J., Gross J., Trela J. and Ferré E. C. (2014) Gabbroic Shergottite Northwest Africa 6963: an intrusive sample of Mars. *Am. Mineral.* **99**, 601–606. https://doi.org/10.2138/am.2014.4638.

Forni O., Gaft M., Toplis M. J., Clegg S. M., Maurice S., Wiens R. C., Mangold N., Gasnault O., Sautter V. and Le Mouélic S. (2015) First detection of fluorine on Mars: implications for Gale crater's geochemistry. *Geophys. Res. Lett.* **42**, 1020–1028.

Fraeman A. A., Ehlmann B. L., Arvidson R. E., Edwards C. S., Grotzinger J. P., Milliken R. E., Quinn D. P. and Rice M. S. (2016) The stratigraphy and evolution of Lower Mt. Sharp from spectra, morphological, and thermophysical orbital datasets. *J. Geophys. Res.* **121**, 1713–1736. https://doi.org/10.1002/2016JE005095.

Fraeman A. A., Arvidson R. E., Catalano J. G., Grotzinger J. P., Morris R. V., Murchie S. L., Stack K. M., Humm D. C., McGovern J. A. and Seelos F. P. (2013) A hematite-bearing layer in Gale crater, Mars: mapping and implications for past aqueous conditions. *Geology* **41**, 1103–1106. https://doi.org/10.1130/G34613.1.

Frydenvang J., Gasda P. J., Hurowitz J. A., Grotzinger J. P., Wiens R. C., Newsom H. E., Edgett K. S., Bridges J. C., Maurice S., Fisk M. R., Johnson J. R., Rapin W., Stein N. T., Clegg S. M., Schwenzer S. P., Bedford C. C., Edwards P. H., Mangold N., Cousin A., Anderson R. B., Payré V., Vaniman D., Blake D. F., Lanza N. L., Gupta S., Van Beek J., Sautter V., Meslin P., Rice M., Milliken R., Gellert R., Thompson L., Clark B. C., Sumner D. Y., Fraeman A. A., Kinch K. M., Madsen M. B., Mirtofanov I. G., Jun I., Calef F. and Vasavada A. R. (2017) Diagenetic silica enrichment and late-stage groundwater activity in Gale crater, Mars. *Geophys. Res. Lett.* **44**, 4716–4724. https://doi.org/10.1002/2017GL073323.

Gellert R., Rieder R., Brückner J., Clark B. C., Dreibus G., Klingelhöfer G., Lugmair G., Ming D. W., Wänke H., Yen A., Zipfel J. and Squyres S. W. (2006) Alpha particle X-Ray spectrometer (APXS): results from Gusev crater and calibration

report. *J. Geophys. Res. Planets* **111**, E02S05. https://doi.org/10.1029/2005JE002555.

Green T. H., Green D. H. and Ringwood A. E. (1967) The origin of high-alumina basalts and their relationships to quartz tholeiites and alkali basalts. *Earth Planet. Sci. Lett.* **2**, 41–51. https://doi.org/10.1016/0012-821X(67)90171-9.

Grotzinger J. P., Gupta S., Malin M. C., Rubin D. M., Schieber J., Siebach K., Sumner D. Y., Stack K. M., Vasavada A. R. and Arvidson R. E. (2015) Deposition, exhumation, and paleoclimate of an ancient lake deposit, Gale crater, Mars. *Science* **350**, aac7575. https://doi.org/10.1126/science.aac7575.

Grotzinger J. P., Crisp J., Vasavada A. R., Anderson R. C., Baker C. J., Barry R., Blake D. F., Conrad P., Edgett K. S., Ferdowski B., Gellert R., Gilbert J. B., Golombek M., Gómez-Elvira J., Hassler D. M., Jandura L., Litvak M., Mahaffy P., Maki J., Meyer M., Malin M. C., Mitrofanov I., Simmonds J. J., Vaniman D., Welch R. V. and Wiens R. C. (2012) Mars science laboratory mission and science investigation. *Space Sci. Rev.* **170**, 5–56. https://doi.org/10.1007/s11214-012-9892-2.

Grotzinger J. P., Sumner D. Y., Kah L. C., Stack K., Gupta S., Edgar L., Rubin D., Lewis K., Schieber J., Mangold N., Milliken R., Conrad P. G., DesMarais D., Farmer J., Siebach K., Calef, 3rd, F., Hurowitz J., McLennan S. M., Ming D., Vaniman D., Crisp J., Vasavada A., Edgett K. S., Malin M., Blake D., Gellert R., Mahaffy P., Wiens R. C., Maurice S., Grant J. A., Wilson S., Anderson R. C., Beegle L., Arvidson R., Hallet B., Sletten R. S., Rice M., Bell, 3rd, J., Griffes J., Ehlmann B., Anderson R. B., Bristow T. F., Dietrich W. E., Dromart G., Eigenbrode J., Fraeman A., Hardgrove C., Herkenhoff K., Jandura L., Kocurek G., Lee S., Leshin L. A., Leveille R., Limonadi D., Maki J., McCloskey S., Meyer M., Minitti M., Newsom H., Oehler D., Okon A., Palucis M., Parker T., Rowland S., Schmidt M., Squyres S., Steele A., Stolper E., Summons R., Treiman A., Williams R., Yingst A. and Team M. S. L. S. (2014) A habitable fluvio-lacustrine environment at Yellowknife Bay, Gale crater, Mars (New York, N.Y.). *Science* **343**, 1242777. https://doi.org/10.1126/science.1242777.

Haddadi B., Sigmarsson O. and Devidal J.-L. (2015) Determining intensive parameters through clinopyroxene-liquid equilibrium in Grímsvötn 2011 and Bárðarbunga 2014 basalts. *Geophys. Res. Abstracts*.

Hamilton V. E. and Christensen P. R. (2005) Evidence for extensive, olivine-rich bedrock on Mars. *Geology* **33**, 433–436. https://doi.org/10.1130/G21258.1.

Hanna R. D., Hamilton V. E. and Putzig N. E. (2016) The complex relationship between olivine abundance and thermal inertia on Mars. *J. Geophys. Res. Planets* **121**, 1293–1320. https://doi.org/10.1002/2015JE004924.

Hausrath E. M., Ming D. W., Peretyazhko T. S. and Rampe E. B. (2018) Reactive transport and mass balance modeling of the Stimson sedimentary formation and altered fracture zones constrain diagenetic conditions at Gale crater, Mars. *Earth Planet. Sci. Lett.* **491**, 1–10. https://doi.org/10.1016/j.epsl.2018.02.037.

Hausrath E. M., Navarre-Stichler A. K., Sak P. B., Steefel C. I. and Brantley S. L. (2008) Basalt weathering rates on Earth and the duration of liquid water on the plains of Gusev Crater, Mars. *Geology* **36**, 67–70. https://doi.org/10.1130/G24238A.1.

Henares S., Bloemsma M. R., Donselaar M. E., Mijnlieff H. F., Redjosentono A. E., Veldkamp H. G. and Weltje G. J. (2014) The role of detrital anhydrite in diagenesis of aeolian sandstones (Upper Rotliegend, The Netherlands): implications for reservoir-quality prediction. *Sed. Geol.* **314**, 60–74. https://doi.org/10.1016/j.sedgeo.2014.10.001.

Herron M. M. (1988) Geochemical classification of terrigenous sands and shales from core or log data. *J. Sediment. Res.* **58**, 820–829.

Hoefen T. M., Clark R. N., Bandfield J. L., Smith M. D., Pearl J. C. and Christensen P. R. (2003) Discovery of olivine in the Nili Fossae region of Mars. *Science* **302**, 627–630. https://doi.org/10.1126/science.1089647.

Humayun M., Nemchin A., Zanda B., Hewins R. H., Grange M., Kennedy A., Lorand J. P., Göpel C., Fieni C., Pont S. and Deldicque D. (2013) Origin and age of the earliest Martian crust from meteorite NWA 7533. *Nature* **503**, 513. https://doi.org/10.1038/nature12764.

Hurowitz J. A., Grotzinger J. P., Fischer W. W., Milliken R., Stein N., Vasavada A. R., Blake D. F., Dehouck E., Eigenbrode J. L., Fairen A. G., Frydenvang J., Gellert R., Grant J. A., Gupta S., Herkenhoff K. E., McLennan S. M., Ming D. W., Rampe E. B., Schmidt M. E., Siebach K., Stack-Morgan K., Sumner D. Y. and Wiens R. C. (2017) Redox stratification of an ancient lake in Gale crater, Mars. *Science* **356**, eeah6849, 10.1126/science.aah6849.

Hynek B. M. and Phillips R. J. (2001) Evidence for extensive denudation of the Martian highlands. *Geology* **29**, 407–410. https://doi.org/10.1130/0091-7613(2001)029<0407:EFEDOT>2.0.CO;2.

Hynek B. M. and Phillips R. J. (2003) New data reveal mature, integrated drainage systems on Mars indicative of past precipitation. *Geology* **31**, 757–760. https://doi.org/10.1130/G19607.1.

Jakobsson S. P. (1972) Chemistry and distribution pattern of recent basaltic rocks in Iceland. *Lithos* **5**, 365–386.

Jin Z., Li F., Cao J., Wang S. and Yu J. (2006) Geochemistry of Daihai Lake sediments, Inner Mongolia, north China: implications for provenance, sedimentary sorting, and catchment weathering. *Geomorphology* **80**, 147–163. https://doi.org/10.1016/j.geomorph.2006.02.006.

Kah L. C., Kronyak R., Van Beek J., Nachon M., Mangold N., Thompson L., Wiens R., Grotzinger J., Farmer J. and Minitti M. (2015) Diagenetic Crystal Clusters and Dendrites, Lower Mount Sharp, Gale crater. *46th Lunar and Planetary Science Conference, Houston, TX, United States*.

Keith T. E. and Muffler L. (1978) Minerals produced during cooling and hydrothermal alteration of ash flow tuff from Yellowstone drill hole Y-5. *J. Volcanol. Geoth. Res.* **3**, 373–402.

Kroonenberg S. B. (1994) Effects of provenance, sorting and weathering on the geochemistry of fluvial sands from different tectonic and climatic environments. In *Proceedings of the 29th International Geological Congress, Part A*, pp. 69–81.

L'Haridon J., Mangold N., Meslin P. Y., Johnson J. R., Rapin W., Forni O., Cousin A., Payré V., Dehouck E., Nachon M., Le Deit L., Gasnault O., Maurice S. and Wiens R. C. (2018) Chemical variability in mineralized veins observed by ChemCam on the lower slopes of Mount Sharp in Gale crater, Mars. *Icarus* **311**, 69–86. https://doi.org/10.1016/j.icarus.2018.01.028.

Le Bas M. J., Maitre R., Streckeisen A. and Zanettin B. (1986) A chemical classification of volcanic rocks based on the total alkali-silica diagram. *J. Petrol.* **27**, 745–750. https://doi.org/10.1093/petrology/27.3.745.

Le Deit L., Mangold N., Forni O., Cousin A., Lasue J., Schröder S., Wiens R. C., Sumner D., Fabre C. and Stack K. M. (2016) The potassic sedimentary rocks in Gale crater, Mars, as seen by ChemCam on board Curiosity. *J. Geophys. Res. Planets* **121**, 784–804. https://doi.org/10.1002/2015JE004987.

Le Mouélic S., Gasnault O., Herkenhoff K. E., Bridges N. T., Langevin Y., Mangold N., Maurice S., Wiens R., Pinet P. and Newsom H. E. (2015) The ChemCam Remote Micro-Imager at

Gale crater: review of the first year of operations on Mars. *Icarus* **249**, 93–107. https://doi.org/10.1016/j.icarus.2014.05.030.

Leveille R. J., Bridges J., Wiens R. C., Mangold N., Cousin A., Lanza N., Forni O., Ollila A., Grotzinger J. and Clegg S. (2014) Chemistry of fracture-filling raised ridges in Yellowknife Bay, Gale crater: window into past aqueous activity and habitability on Mars. *J. Geophys. Res. Planet.* **119**, 2398–2415. https://doi.org/10.1002/2014JE004620.

Malin M. C. and Edgett K. S. (2000) Sedimentary rocks of early mars. *Science* **290**, 1927–1937. https://doi.org/10.1126/science.290.5498.1927.

Malin M. C., Ravine M. A., Caplinger M. A., Tony G. F., Schaffner J. A., Maki J. N., Bell J. F., Cameron J. F., Dietrich W. E., Edgett K. S., Edwards L. J., Garvin J. B., Hallet B., Herkenhoff K. E., Heydari E., Kah L. C., Lemmon M. T., Minitti M. E., Olson T. S., Parker T. J., Rowland S. K., Schieber J., Sletten R., Sullivan R. J., Sumner D. Y., Aileen Y. R., Duston B. M., McNair S. and Jensen E. H. (2017) The mars science laboratory (msl) mast cameras and descent imager: investigation and instrument descriptions. *Earth Space Sci.* **4**, 506–539. https://doi.org/10.1002/2016EA000252.

Mangold N., Forni O., Dromart G., Stack K., Wiens R. C., Gasnault O., Sumner D. Y., Nachon M., Meslin P. Y. and Anderson R. B. (2015) Chemical variations in Yellowknife Bay formation sedimentary rocks analyzed by ChemCam on board the Curiosity rover on Mars. *J. Geophys. Res. Planets* **120**, 452–482.

Mangold N., Thompson L. M., Forni O., Williams A. J., Fabre C., Le Deit L., Wiens R. C., Williams R., Anderson R. B. and Blaney D. L. (2016) Composition of conglomerates analyzed by the Curiosity rover: Implications for Gale Crater crust and sediment sources. *J. Geophys. Res. Planets* **121**, 353–387. https://doi.org/10.1002/2015JE004977.

Mangold N., Dehouck E., Forni O., Le Deit L., Rivera-Hernandez F., L'Haridon J., Frydevang J., Meslin P.-Y., McLennan S. M. and Newsom H. E. (2017a) Aqueous Alteration in Mt. Sharp Mudstones Evidenced by ChemCam, Curiosity. *48th Lunar and Planetary Science Conference, Houston, TX, United States*.

Mangold N., Schmidt M. E., Fisk M. R., Forni O., McLennan S. M., Ming D., Sautter V., Sumner D., Williams A. J. and Clegg S. M. (2017b) Classification scheme for sedimentary and igneous rocks in Gale crater, Mars. *Icarus* **284**, 1–17. https://doi.org/10.1016/j.icarus.2016.11.005.

Mangold N., Dehouck E., Fedo C., Forni O., Achilles C. N., Bristow T. F., Frydenvang J., Gasnault O., L'Haridon J., Le Deit L., Maurice S., McLennan S. M., Meslin P. Y., Morrison S. M., Newsom H., Rampe E. B., Rivera-Hernandez F., Salvatore M. and Wiens R. (2018) Open-system weathering on Mars from the chemistry of mudstones at Gale crater. *Icarus*.

Maurice S., Wiens R. C., Saccoccio M., Barraclough B., Gasnault O., Forni O., Mangold N., Baratoux D., Bender S. and Berger G. (2012) The ChemCam instrument suite on the Mars Science Laboratory (MSL) rover: science objectives and mast unit description. *Space Sci. Rev.* **170**, 95–166. https://doi.org/10.1007/s11214-012-9912-2.

Maurice S., Clegg S. M., Wiens R. C., Gasnault O., Rapin W., Forni O., Cousin A., Sautter V., Mangold N. and Le Deit L. (2016) ChemCam activities and discoveries during the nominal mission of the Mars Science Laboratory in Gale crater, Mars. *J. Anal. At. Spectrom.* **31**, 863–889. https://doi.org/10.1039/C5JA00417A.

McCubbin F. M., Nekvasil H., Harrington A. D., Elardo S. M. and Lindsley D. H. (2008) Compositional diversity and stratification of the Martian crust: inferences from crystallization experiments on the picrobasalt Humphrey from Gusev Crater, Mars. *J. Geophys. Res.: Planet.* **113**, E11013. https://doi.org/10.1029/2008JE003165.

McKinley J. M., Atkinson P. M., Lloyd C. D., Ruffell A. H. and Worden R. H. (2011) How porosity and permeability vary spatially with grain size, sorting, cement volume, and mineral dissolution in fluvial triassic sandstones: the value of geostatistics and local regression. *J. Sediment. Res.* **81**, 844–858. https://doi.org/10.2110/jsr.2011.71.

McLennan S. M. (2003) Sedimentary silica on Mars. *Geology* **31**, 315–318. https://doi.org/10.1130/0091-7613(2003) 031<0315:SSOM>2.0.CO;2.

McLennan S. M., Dehouck E., Grotzinger J. P., Hurowitz J. A., Mangold N. and Siebach K. (2015) Geochemical record of open-system chemical weathering at Gale Crater and implications for paleoclimates on Mars. *46th Lunar and Planetary Science Conference, Houston, TX, United States*.

McLennan S. M., Anderson R., Bell J., Bridges J., Calef F., Campbell J. L., Clark B., Clegg S., Conrad P. and Cousin A. (2014) Elemental geochemistry of sedimentary rocks at Yellowknife Bay, Gale crater, Mars. *Science* **343**, 1244734. https://doi.org/10.1126/science.1244734.

McSween H. Y., Taylor G. J. and Wyatt M. B. (2009) Elemental composition of the Martian crust. *Science* **324**, 736–739. https://doi.org/10.1126/science.1165871.

McSween H. Y., Ruff S. W., Morris R. V., Bell J., Herkenhoff K., Gellert R., Stockstill K. R., Tornabene L. L., Squyres S. W. and Crisp J. A. (2006) Alkaline volcanic rocks from the Columbia Hills, Gusev crater, Mars. *J. Geophys. Res. Planets* **111**, 2156–2202. https://doi.org/10.1029/2006JE002698.

Meslin P.-Y., Gasnault O., Forni O., Schröder S., Cousin A., Berger G., Clegg S., Lasue J., Maurice S. and Sautter V. (2013) Soil diversity and hydration as observed by ChemCam at Gale Crater, Mars. *Science* **341**, 1238670.

Meslin P. Y., Gasda P. J., Haridon J. L., Forni O., Lanza N., Lamm S., Johnson J. R., Wiens R. and Thompson L. (2018) Detection of hydrous manganese and iron oxides with variable phosphorous and magnesium contents in the lacustrine sediments of the Murray formation, Gale, Mars. *49th Lunar and Planetary Science Conference, Houston, Texas, USA*.

Milliken R. E., Grotzinger J. P. and Thomson B. J. (2010) Paleoclimate of Mars as captured by the stratigraphic record in Gale Crater. *Geophys. Res. Lett.* **37**, L04201. https://doi.org/10.1029/2009GL041870.

Morris R. V., Vaniman D. T., Blake D. F., Gellert R., Chipera S. J., Rampe E. B., Ming D. W., Morrison S. M., Downs R. T., Treiman A. H., Yes A. S., Grotzinger J. P., Achilles C. N., Bristow T. F., Crisp J. A., Des Marais D., Farmer J. D., Fendrich K. V., Frydenvang J., Graff T. G., Morookian J.-M., Stolper E. M. and Schwenzer S. P. (2016) Silicic volcanism on Mars evidenced by tridymite in high-SiO2 sedimentary. In *rock at Gale crater. Proceedings of the National Academy of Sciences*, pp. 7071–7076. https://doi.org/10.1073/pnas.1607098113.

Morrison S. M., Downs R. T., Blake D. F., Vaniman D. T., Ming D. W., Rampe E. B., Bristow T. F., Achilles C. N., Chipera S. J., Yen A. S., Morris R. V., Treiman A. H., Hazen R. M., Sarrazin P. C., Gellert R., Fendrich K. V., Morookian J.-M., Farmer J. D., Des Marais D. and Craig P. I. (2018) Crystal Chemistry of Martian Minerals from Bradbury Landing through Naukluft Plateau. American Mineralogist, Gale crater, Mars, 10.2138/am2018-6124.

Nachon M., Clegg S. M., Mangold N., Schröder S., Kah L. C., Dromart G., Ollila A., Johnson J. R., Oehler D. Z. and Bridges J. C. (2014) Calcium sulfate veins characterized by ChemCam/Curiosity at Gale crater, Mars. *J. Geophys. Res. Planets* **119**, 1991–2016. https://doi.org/10.1002/2013JE004588.

Nachon M., Mangold N., Forni O., Kah L. C., Cousin A., Wiens R. C., Anderson R., Blaney D., Blank J. G. and Calef F. (2017) Chemistry of diagenetic features analyzed by ChemCam at

Pahrump Hills, Gale crater, Mars. *Icarus* **281**, 121–136. https://doi.org/10.1016/j.icarus.2016.08.026.

Nesbitt H. W. and Wilson R. E. (1992) Recent chemical weathering of basalts. *Am. J. Sci.* **292**, 740–777. https://doi.org/10.2475/ajs.292.10.740.

Nesbitt H. W. and Young G. M. (1982) Early Proterozoic climates and plate motions inferred from major element chemistry of lutites. *Nature* **299**, 715–717.

Nesbitt H. W. and Young G. M. (1996) Petrogenesis of sediments in the absence of chemical weathering: effects of abrasion and sorting on bulk composition and mineralogy. *Sedimentology* **43**, 341–358. https://doi.org/10.1046/j.1365-3091.1996.d01-12.x.

Neter J., Kutner M., Nachtsheim C. and Wasserman W. (1996) Applied Linear Statistical Models. Irwin, Chicago.

Pettijohn F. (1954) Classification of sandstones. *J. Geol.* **62**, 360–365.

Pettijohn F. J., Potter P. E. and Siever R. (1972) Sand and Sandstones, 1–618. Springer, Berlín.

Rampe E. B., Ming D. W., Blake D. F., Bristow T. F., Chipera S. J., Grotzinger J. P., Morris R. V., Morrison S. M., Vaniman D. T. and Yen A. S. (2017a) Mineralogy of an ancient lacustrine mudstone succession from the Murray formation, Gale crater, Mars. *Earth Planet. Sci. Lett.* **471**, 172–185. https://doi.org/10.1016/j.epsl.2017.04.021.

Rampe E. B., Ming D. W., Grotzinger J. P., Morris R. V., Blake D. F., Vaniman D. T., Bristow T. F., Morrison S. M., Yen A. S. and Chipera S. J. (2017b) Mineral trends in early hesperian lacustrine mudstone at gale crater, mars. *48th Lunar and Planetary Science, Houston, TX, United States*.

Rapin W., Meslin P.-Y., Maurice S., Vaniman D., Nachon M., Mangold N., Schröder S., Gasnault O., Forni O., Wiens R. C., Martinez G. M., Cousin A., Sautter V., Lasue J. and Rampe E. B. (2016) Hydration state of calcium sulfates in Gale crater, Mars: identification of bassanite veins. *Earth Planet. Sci. Lett.* **452**, 197–205. https://doi.org/10.1016/j.epsl.2016.07.045.

Roser B. P. and Korsch R. J. (1986) Determination of tectonic setting of sandstone-mudstone suites using content and ratio. *J. Geol.* **94**, 635–650. https://doi.org/10.1086/629071.

Sautter V., Toplis M., Wiens R., Cousin A., Fabre C., Gasnault O., Maurice S., Forni O., Lasue J. and Ollila A. (2015) In situ evidence for continental crust on early Mars. *Nat. Geosci.* **8**, 605–609. https://doi.org/10.1038/ngeo2474.

Sautter V., Fabre C., Forni O., Toplis M. J., Cousin A., Ollila A. M., Meslin P. Y., Maurice S., Wiens R. C. and Baratoux D. (2014) Igneous mineralogy at Bradbury Rise: the first ChemCam campaign at Gale crater. *J. Geophys. Res. Planets* **119**, 30–46. https://doi.org/10.1002/2013JE004472.

Schieber J., Bish D., Coleman M., Reed M., Hausrath E. M., Cosgrove J., Gupta S., Minitti M., Edgett K., Malin M. C. and Sheldon N. (2017) Encounters with an unearthly mudstone: understanding the first mudstone found on Mars. *Sedimentology* **64**, 311–358. https://doi.org/10.1111/sed.12318.

Schwenzer S. P., Bridges J. C., Wiens R. C., Conrad P. G., Kelley S. P., Leveille R., Mangold N., Martín-Torres J., McAdam A. and Newsom H. (2016) Fluids during diagenesis and sulfate vein formation in sediments at Gale crater, Mars. *Meteorit. Planet. Sci.* **51**, 2175–2202. https://doi.org/10.1111/maps.12668.

Shinohara Y. and Kohyama N. (2004) Quantitative analysis of tridymite and cristobalite crystallized in rice husk ash by heating. *Ind. Health* **42**, 277–285. https://doi.org/10.2486/indhealth.42.277.

Siebach K. L., Baker M. B., Grotzinger J. P., McLennan S. M., Gellert R., Thompson L. M. and Hurowitz J. A. (2017) Sorting out compositional trends in sedimentary rocks of the bradbury group (Aeolus Palus), Gale Crater, Mars. *J. Geophys. Res. Planets* **122**, 295–328. https://doi.org/10.1002/2016JE005195.

Smith M. R. and Bandfield J. L. (2012) Geology of quartz and hydrated silica-bearing deposits near Antoniadi Crater, Mars. *J. Geophys. Res.: Planets* **117**, E06007. https://doi.org/10.1029/2011JE004038.

Stack K. M., Edwards C. S., Grotzinger J. P., Gupta S., Sumner D. Y., Calef F. J., Edgar L. A., Edgett K. S., Fraeman A. A., Jacob S. R., Le Deit L., Lewis K. W., Rice M. S. and Rubin D. (2016) Comparing orbiter and rover image-based mapping of an ancient sedimentary environment, Aeolis Palus, Gale crater, Mars. *Icarus* **280**, 3–21. https://doi.org/10.1016/j.icarus.2016.02.024.

Stack K. M., Grotzinger J. P., Griffes J. L. and Farley R. N. (2014a) Global Distribution of Stratified Deposits on Mars. In *STRATI 2013: First International Congress on Stratigraphy At the Cutting Edge of Stratigraphy* (eds. R. Rocha, J. Pais, J. C. Kullberg and S. Finney). Springer International Publishing, Cham, pp. 361–364.

Stack K. M., Grotzinger J. P., Kah L. C., Schmidt M. E., Mangold N., Edgett K. S., Sumner D. Y., Siebach K. L., Nachon M., Lee R., Blaney D. L., Deflores L. P., Edgar L. A., Fairén A. G., Leshin L. A., Maurice S., Oehler D. Z., Rice M. S. and Wiens R. C. (2014b) Diagenetic origin of nodules in the Sheepbed member, Yellowknife Bay formation, Gale crater, Mars. *J. Geophys. Res. Planets* **119**, 1637–1664. https://doi.org/10.1002/2014JE004617.

Thompson L. M., Schmidt M. E., Spray J. G., Berger J. A., Fairén A. G., Campbell J. L., Perrett G. M., Boyd N., Gellert R. and Pradler I. (2016) Potassium-rich sandstones within the Gale impact crater, Mars: the APXS perspective. *J. Geophys. Res. Planets* **121**, 1981–2003. https://doi.org/10.1002/2016JE005055.

Thomson B. J., Bridges N. T., Milliken R., Baldridge A., Hook S. J., Crowley J. K., Marion G. M., de Souza Filho C. R., Brown A. J. and Weitz C. M. (2011) Constraints on the origin and evolution of the layered mound in Gale Crater, Mars using Mars Reconnaissance Orbiter data. *Icarus* **214**, 413–432. https://doi.org/10.1016/j.icarus.2011.05.002.

Tolosana-Delgado R. and von Eynatten H. (2009) Grain-size control on petrographic composition of sediments: compositional regression and rounded zeros. *Math. Geosci.* **41**, 869–886. https://doi.org/10.1007/s11004-009-9216-6.

Treiman A. H., Bish D. L., Vaniman D. T., Chipera S. J., Blake D. F., Ming D. W., Morris R. V., Bristow T. F., Morrison S. M. and Baker M. B. (2016) Mineralogy, provenance, and diagenesis of a potassic basaltic sandstone on Mars: CheMin X-ray diffraction of the Windjana sample (Kimberley area, Gale Crater). *J. Geophys. Res. Planets* **121**, 75–106. https://doi.org/10.1002/2015JE004932.

Vaniman D., Dyar M. D., Wiens R., Ollila A., Lanza N., Lasue J., Rhodes J. M., Clegg S. and Newsom H. (2012) Ceramic ChemCam calibration targets on Mars Science Laboratory. *Space Sci. Rev.* **170**, 229–255. https://doi.org/10.1007/s11214-012-9886-0.

Vaniman D., Bish D., Ming D., Bristow T., Morris R., Blake D., Chipera S., Morrison S., Treiman A. and Rampe E. (2014) Mineralogy of a mudstone at Yellowknife Bay, Gale crater, Mars. *Science* **343**, 1243480.

Vaniman D., Martinez G. M., Rampe E. B., Bristow T. F., Blake D. F., Yen A. S., Ming D. W., Rapin W., Meslin P. Y., Morookian J. M., Downs R. T., Chipera S. J., Morris R. V., Morrison S. M., Treiman A. H., Achilles C. N., Robertson K., Grotzinger J., Hazen R. M. and Wiens R. (2018) Gypsum, bassanite, and anhydrite at Gale crater, Mars. *Geology*.

Vasavada A. R., Grotzinger J. P., Arvidson R. E., Calef F. J., Crisp J. A., Gupta S., Hurowitz J., Mangold N., Maurice S. and Schmidt M. E. (2014) Overview of the mars science laboratory

mission: bradbury landing to yellowknife bay and beyond. *J. Geophys. Res. Planets* **119**, 1134–1161. https://doi.org/10.1002/2014JE004622.

Weltje G. J. (2012) Quantitative models of sediment generation and provenance: state of the art and future developments. *Sed. Geol.* **280**, 4–20. https://doi.org/10.1016/j.sedgeo.2012.03.010.

Wiens R. C., Maurice S., Barraclough B., Saccoccio M., Barkley W. C., Bell Iii J. F., Bender S., Bernardin J., Blaney D. and Blank J. (2012) The ChemCam instrument suite on the Mars Science Laboratory (MSL) rover: body unit and combined system tests. *Space Sci. Rev.* **170**, 167–227. https://doi.org/10.1007/s11214-012-9902-4.

Wiens R. C., Maurice S., Lasue J., Forni O., Anderson R. B., Clegg S., Bender S., Blaney D., Barraclough B. L. and Cousin A. (2013) Pre-flight calibration and initial data processing for the ChemCam laser-induced breakdown spectroscopy instrument on the Mars Science Laboratory rover. *Spectrochim. Acta, Part B* **82**, 1–27. https://doi.org/10.1016/j.sab.2013.02.003.

Williams R., Sumner D., Gupta S., Grotzinger J., Rubin D., Edgett K., Rice M., Edgar L., Lewis K. and Minitti M. (2014) Sedimentology of Darwin waypoint from Curiosity observations. *Lunar Planet. Sci. Conf.*, 2401.

Yen A. S., Ming D. W., Vaniman D. T., Gellert R., Blake D. F., Morris R. V., Morrison S. M., Bristow T. F., Chipera S. J. and Edgett K. S. (2017) Multiple stages of aqueous alteration along fractures in mudstone and sandstone strata in Gale Crater, Mars. *Earth Planet. Sci. Lett.* **471**, 186–198. https://doi.org/10.1016/j.epsl.2017.04.033.

Associate editor: Jeffrey G Catalano